Department of Physics and Astronomy
University of Heidelberg

Bachelor Thesis in Physics
submitted by

Thomas Federico Rösch

born in Heidelberg (Germany)

August 2013

Using the Blue/Green Emission in Fluorescent Nuclear Track Detectors for Ion Beam Therapy Research

This Bachelor Thesis has been carried out by Thomas Federico Rösch at the
German Cancer Research Center (DKFZ) in Heidelberg
under the supervision of
Prof. Dr. rer. nat. Peter Bachert
and
Prof. Dr. rer. nat. Oliver Jäkel

Kurzfassung

Zur Erforschung der Mechanismen der Protonen- und Ionentherapie benötigt man Detektoren, die in der Lage sind Energiedepositionen auf Skalen von Mikro- bis Nanometern zu quantifizieren. Auf dotiertem Aluminiumoxid basierende Fluoreszierende Kernspurdetektoren (FNTDs) sind dazu fähig. Die Tatsache, dass deren Konzentration an fluoreszierenden Farbzentren sowohl von Detektor zu Detektor, als auch innerhalb eines Detektors stark schwanken kann, kann die Anwendung der FNTDs erschweren. Deshalb befasst sich diese Arbeit mit dem Zusammenhang zwischen der häufig genutzten Fluoreszenz mit roter Absorptionsbande und der bisher ungenutzten Fluoreszenz mit blauer Absorption und den dazugehörigen Farbzentren, sowie mit dessen Einfluss auf die Detektorsensitivität. Es soll auch die Möglichkeit eingeschätzt werden die bisher ungenutzte blau-grüne Fluoreszenz (blauer Kanal) zur Quantifizierung und Normalisierung zu benutzen. Die Versuche wurden hauptsächlich an einer Reihe von 20 handverlesenen FNTDs durchgeführt, die das während der Kristallzüchtung auftauchende Spektrum an Kristallfarben abdecken. Es wurde gezeigt, dass ein konsistentes Auslesen des blauen Kanals mit den Standardmethoden möglich ist. Das blaue Signal vor Bestrahlung (und bis zu einer Dosis von 10 Gy) ist ein gutes Maß für die Gesamtkonzentration an Farbzentren. Sowohl Detektorsensitivität als auch der Hintergrund (vor Bestrahlung) sind signifikant mit dem blauen Signal nach Bestrahlung korreliert und erlauben dadurch eine Normalisierung unterschiedlicher Proben. Außerdem wurde eine neue laserabhängige Signalabnahme gefunden, dessen Folgen für die Dosimetrie noch nicht eingeschätzt werden können. Auch konnte beobachtet werden, dass einfache optische Absorptionsmessungen der Farbe der Detektoren nicht direkte Messungen des blauen Kanals ersetzen können.

Abstract

For studies on the mechanisms of proton and ion radiotherapy it is necessary to have a detector able to quantify local energy deposition on nano- to micrometer scales. Fluorescent nuclear track detectors (FNTDs) based on biocompatible doped alumina single crystals fulfill these criteria. However, the concentration of fluorescent color centers can vary from detector to detector and even within the same sample. This can hamper severely the application of FNTDs. This work's purpose was therefore to investigate the relations between (usually used) red/near IR and (hitherto unused) blue/green fluorescence and corresponding color center concentrations and their influence on the detector sensitivity as well as to assess the feasibility of employing the blue-greenish fluorescence (blue channel) for quantification and normalization. The study was mainly done on a set of 20 differently colored, hand-selected unirradiated FNTDs representing the span of coloration found during the crystal growth process. We found out that is feasible to read out the blue channel consistently with our standard equipment. The blue/green fluorescence before irradiation (and after until 10 Gy) is a good measure for the total color center concentration. Both the sensitivity and the background (before irradiation) were found to correlate significantly with the blue signal after irradiation, allowing for normalization of intersample variability. We did not find saturation of blue signal for doses up to 10 kGy which might open the use of FNTD for high dose measurements. New laser dependent color center depletion was discovered with yet unclear implications for dosimetry. We also found that simple optical absorption measurements for coloration do not replace blue channel measurements.

Contents

1. Introduction

While conventional radiation therapy with high energy photons has been established in clinics for a long time, radiation therapy with swift heavy charged particles (HCPs), *e.g.* protons and carbon ions, has increased in popularity over the recent decade. The physical advantages are an inverse dose profile with a defined range and high local dose deposition (Bragg Peak) yielding a high dose conformitiy and hence a better differential effect between tumor and healthy tissue. Futhermore, HCPs have a better relative biological effectiveness (RBE) as compared to MV photons due to an enhanced linear energy transfer (LET) and large local dose variation [1]. Thus for studies on the mechanisms of proton and ion radiotherapy it is necessary to have a detector able to quantify local energy deposition on nano- to micrometer scales. Fluorescent nuclear track detectors (FNTDs) based on biocompatible alumina single crystals doped with carbon and magnesium and read out by laser scanning confocal microscopy [2], fulfil these criteria. FNTDs allow diffraction-limited 3D imaging of energy deposition and have recently been introduced as a tool for ion beam therapy research [3].

When exposed to ionizing radiation, FNTDs undergo a radiochromatic transformation, *i.e.* unirradiated color centers show fluorescence in the blue-green wavelength range, whereas transformed centers emit in the near infrared. Due to inevitable processes during the crystal production the concentrations of color centers differ between detectors and maybe even within single detectors, causing a highly variable signal background (*i.e.* transformed centers in unirradiated crystals) and variation in sensitivity (*i.e.* fluorescence signal per dose). This can hamper severely the application of FNTDs for dosimetry and particle type/energy discrimination in ion beams.

This work's purpose was therefore to investigate the relations between transformed and untransformed color center concentrations and their influence on the detector sensitivity as well as to assess the feasibility of employing the hitherto unused blue-greenish fluorescence for quantification and normalization. The study was mainly done on a set of 20 hand-selected unirradiated FNTDs, representing the range of coloration found during the crystal growth process tested.

A detailed description of the experiments can be found in chapter 4. Physical and other background will be explained in chapter 2. Chapter 3 refers to the used hard- and software and chapter 5 presents the experiments and results. Finally, the chapters 6 and 7 complete this work with dicussion of the results and a conclusion.

2. Background

2.1. Ionizing Radiation

Radiation of particles or electromagnetic waves with energies high enough to remove an electron from the atomic orbit is called ionizing radiation. Particles as well as photons are used in radiation therapy to produce ionization in tumor cells. The resulting radicals cause damage to the DNA which drives cells into inactivation.
When an ionizing particle hits matter atomic and nuclear interactions (depending on the projectile and target) transfer the particles energy to the target. The measure of energy deposited in matter is denominated absorbed dose D and is defined by the International Commission on Radiation Units and Measurements (ICRU) as

$$D := \frac{d\bar{\epsilon}}{dm} \, [\mathrm{J\,kg^{-1}}] \tag{2.1}$$

where $d\bar{\epsilon}$ is the mean energy imparted to matter of mass dm. The Unit of absorbed dose has the special name gray (Gy) [4].

2.2. Luminescence

Luminescence is a property of materials transforming energy into visible electromagnetic radiation. Whereas luminescence can be initiated by many different types of energy the FNTDs used in this study are photoluminescent crystals. After undergoing radiochromatic transformation they yield fluorescence when being exited with photons. Fluorescence is a subclass of luminescence discriminated from the other subclass by the lifetime of the energy re-emission process. For long lifetimes with transition rates around

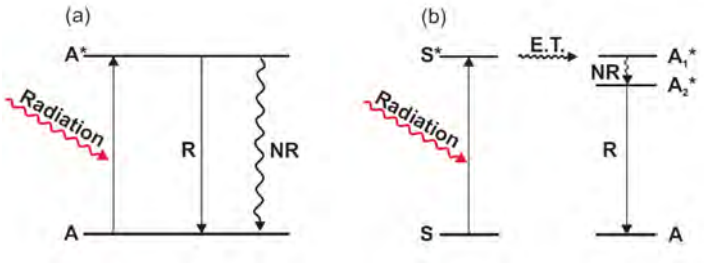

Figure 2.1.: Schematic energy levels for luminescence transitions. Reprinted from [5] according to [6].

10^4 up to $\leq$1 per second the effect is called phosphorescence whereas for short lifetimes (transition rates between 10^7-10^8 per s) it is denominated fluorescence. However, Phosphorescence will not be discussed in detail here.
Luminescent materials generally consist of a host lattice and a luminescent center, also called activator. Incoming radiation raises the activator A to an exited state A^*. The excitation process is dependent on the radiation energy. Ultraviolet and/or visible radiation excites directly (Fig. 2.1(a)), whereas high-energy radiation (*e.g.* gamma-rays) excites indirectly via the host lattice, in this case called sensitizer S. Generally the sensitizer absorbs the incoming energy and transfers it to the activator (Fig. 2.1(b)). A back transfer to the S^* state is prevented by a non-radiative decay in a lower activated state A_2^*. When returning to the ground state A, its additional energy is released as emission of radiation or by transferring heat to the host lattice. The latter is called a non-radiative return (NR)[6].

Stokes shift

In an FNTD the fluorescence emission spectrum is shifted towards lower wavelengths than the absorption spectrum. This phenomenon is observed frequently in fluorescent materials and is called Stokes Shift. It is due to non-radiative transitions between vibrational energy levels in the exited and ground state. Absorption excites the activator into a higher vibrational energy level which then decays into the vibrational ground state. The rate of such a process is in the order of $10^{13}\,\mathrm{s}^{-1}$, thus much faster than emission of radiation having a rate of about $10^8\,\mathrm{s}^{-1}$. Then, the system returns to an exited vibrational level of the ground state. This decay is spontaneous and under emission of radiation (fluorescence). The resulting energy difference between the emission and absorption spectra leads to the Stokes Shift.

2.3. Lambert-Beer Law

The optical absorption of a material can be determined by using Lambert-Beer's law. It states that the initial intensity of light I_0 decreases exponentially when passing through a substance of length l. The transmission T, *i.e.* the ratio of initial and absorbed light, depends logarithmically on the product of l and the substances absorption coefficient α.

$$I = I_0\, e^{-\alpha l} \tag{2.2}$$

$$\ln\left(\frac{I}{I_0}\right) = \ln\left(T\right) = \ln(-\alpha l) \tag{2.3}$$

Hence, by measuring the transmission it is possible to determine the absorption coefficient which is directly correlated to the concentration c of absorbing centers via the extinction coefficient ϵ.

$$\alpha = \frac{\epsilon c}{\ln(10)} \tag{2.4}$$

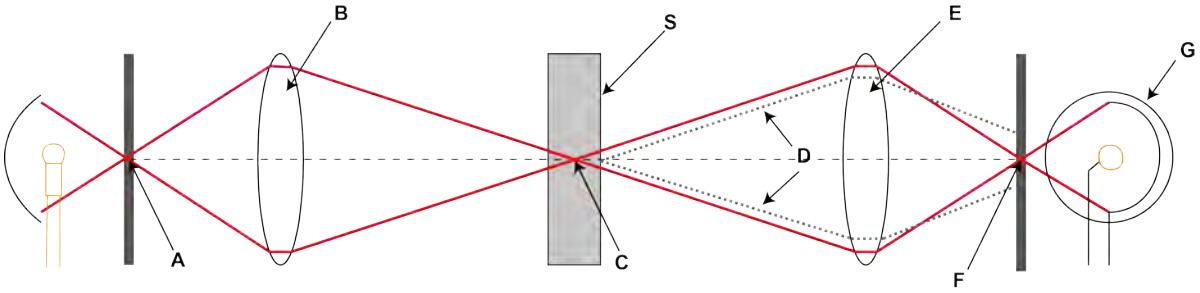

Figure 2.2.: Light path in a confocal microscope after Minsky, M. A, F: pinholes. B, E: confocal lenses. C: Focus. D: light path from other than the focal plane. G: light detector S: specimen. Reproduction according to [7]

2.4. Confocal Microscopy

In a confocal microscope the light is guided through a small aperture called pinhole and then focused to one spot in the specimen. A second lens, placed confocally to the first one, projects the image from the specimen on a second pinhole. This filters out all the light coming from other planes than from the focal one. However, in reality the finite pinhole diameter causes detection of light emitted from planes before and behind the focal plane leading to an effective slice thickness of the regarded volume. To obtain a confocal image of a larger area, it is necessary to scan the area using mirrors which move the focal spot in x and y direction. By moving the specimen along the microscope z-axis the focal plane can be moved through the sample allowing selection of a readout depth.

3. Materials and Methods

3.1. Fluorescent Nuclear Track Detectors - FNTDs

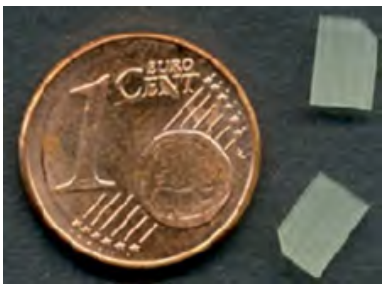

Figure 3.1.: Size of a FNTD compared to a cent coin.

Fluorescent nuclear track detectors, as developed by the Crystal Growth Division of Landauer, Inc. (Stillwater, Oklahoma, U.S.A.), consist of single aluminum oxide crystals doped with carbon and magnesium (Al_2O_3:C,Mg). Because of this doping, they contain a high number of aggregate oxygen vacancy defects leading to the development of aggregate F_2^{2+}(2Mg) color centers (F-centers) during crystal growth. These color centers exhibit radiochromatic transformation under ionizing radiation and therefore FNTDs are able to detect swift heavy charged particles with high efficiency. The detectors are cut out of the single crystal along the optical c-axis into small rectangular plates (4 x 8 x 0.5 mm^3) and are polished on one of the large sides to obtain an optically transparent surface. They are suitable for non-destructive multiple readouts by confocal fluorescence microscopy even a long time after irradiation. [2]

3.1.1. Crystal structure

Aluminum oxide (α-Al_2O_3), also called sapphire or corundum, has a very rigid crystal structure. Its O^{2-}-ions form a slightly distorted, hexagonal-close-packed sublattice with Al^{3+} occupying two out of every three octahedral lattice sides, so that each O^{2-} is surrounded by four tetrahedral nearest-neighbor Al^{3+}-ions [8]. By doping with carbon and magnesium and using a highly reduced atmosphere having low partial pressure of oxygen during crystal growth, oxygen vacancies are introduced in the crystal with a double positive charge (2+) with respect to the lattice. These unoccupied vacancies are denominated as F^{2+} centers. They are able to capture up to two electrons and turn to

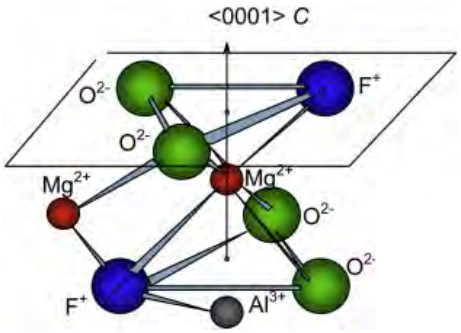

Figure 3.2.: Schematic structure of a F_2^{2+}(2Mg)-center reprinted from [2].

F^+- and (neutral) F-centers respectively. In the presence of Mg^{2+}-ions the formation of aggregate color centers is favored in terms of charge compensation. An aggregate of two F^+-centers is compensated with two Mg-ions and denoted as F_2^{2+}(2Mg)-center (Fig. 3.2). F_2^+(Mg)-centers charge-compensated by one Mg-ion are formed by one F^+-center and one neutral F-center. These aggregates make the crystal useful as radiophotoluminescent detectors and enable a non-destructive readout. Under ionizing radiation secondary electrons are produced in the crystal and are captured by F_2^{2+}(2Mg)-centers, which then transform to F_2^+(2Mg)-centers yielding a different absorption behavior. But as the presence of these aggregate color centers depends on the crystal growth process, their concentration and hence the detectors sensitivity strongly differs within the single crystal [9].

3.1.2. Optical Absorption and Fluorescence

For the investigation of radiation effects the main used defect is the F_2^{2+}(2Mg)-center. It shows a strong absorption band at 435 nm (2.85 eV) with a very short lifetime of (9 ± 3) ns, causing the crystal to appear with a yellow-greenish coloration. The resulting fluorescence has a wavelength of 520 nm. After transformation according to

$$F_2^{2+}(2\mathrm{Mg}) + e^- \rightarrow F_2^+(2\mathrm{Mg}) \tag{3.1}$$

the F_2^+(2Mg)-centers have absorption bands at 620 nm and 335 nm both yielding fluorescence at 750 nm with a short lifetime of (75 ± 5) ns. Transformed color centers are stable and can only be destroyed by heating the detector above 700 °C allowing for multiple readout processes [10].

3.1.3. Writing Process

It is possible to write information in an Al_2O_3:C,Mg crystal by either sequential two-photon absorption (2PA) or ionizing radiation. These processes are illustrated in Fig. 3.3 (left image). The 2PA consists of a first photon having a wavelength in the F_2^{2+}(2Mg) absorption band (435 ± 40) nm and exiting an electron to an intermediate state with a lifetime of about 9 ns. A second photon with the same energy reaching within this

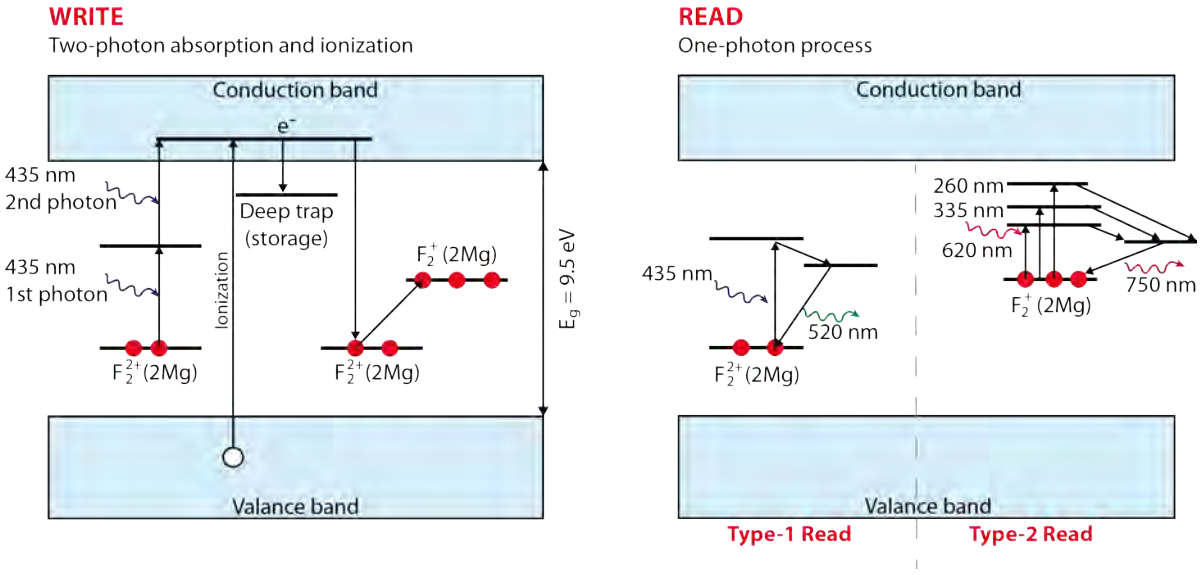

Figure 3.3.: Band diagram of Al_2O_3:C,Mg during reading and writing processes. Reproduction according to [5] and [10].

lifetime can further excite the electron to the conduction band. This process is described by the following equations:

$$F_2^{2+}(2Mg) + \hbar\omega_1 \rightarrow F_2^{2+}(2Mg)^* \tag{3.2}$$

$$F_2^{2+}(2Mg)^* + \hbar\omega_1 \rightarrow F_2^{3+}(2Mg) + e^- \quad . \tag{3.3}$$

The conduction band electron falls now either into long storing deep traps or another $F_2^{2+}(2Mg)$, causing photochromatic transformation resulting in the formation of a $F_2^{+}(2Mg)$-center.

$$F_2^{2+}(2Mg) + e^- \rightarrow F_2^{+}(2Mg) \tag{3.4}$$

$F_2^{2+}(2Mg)$ undergo the same transformation when capturing electrons of an electron-hole pair released by ionizing radiation [10, 11].

3.1.4. Readout Process

For reading out the detectors, two non-destructive fluorescent processes are feasible. Both are illustrated in Fig. 3.3 (right image). The Type-1 readout, also referred to as "negative" readout, addresses untransformed $F_2^{2+}(2Mg)$-centers. This center is exited with (435 ± 40) nm blue laser light using low intensities in order to not induce 2PA processes. The term "negative" is used, because transformed centers exhibit lower intensities of fluorescent light than untransformed ones. For the Type-2, or "positive" readout, transformed $F_2^{+}(2Mg)$-centers are used. Exited with (335 ± 30) nm or (620 ± 50) nm, they yield fluorescence at 750 nm with a lifetime of (75 ± 5) ns. This short lifetime and the deep trapped electrons enable fast and multiple readouts without ionization [10].

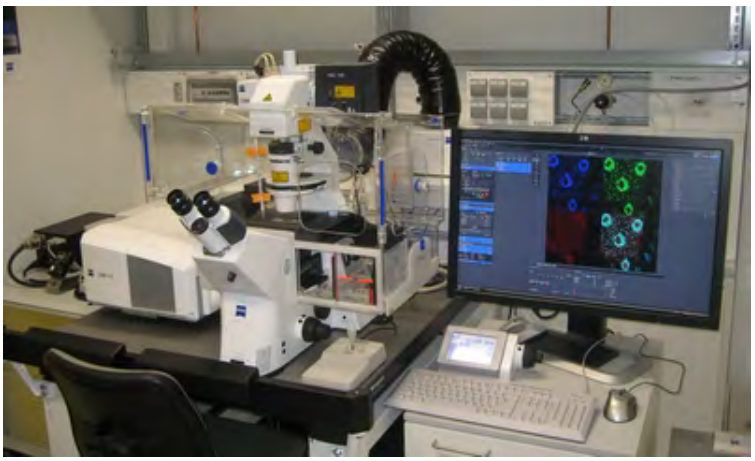

Figure 3.4.: Zeiss LSM 710 ConfoCor 3, Light microscopy facility, DKFZ.

In the following the term "readout" always refers to the measurement of a FNTDs fluorescence signal with the Zeiss LSM 710. The Type-1 readout and the Type-2 readout shall be denominated "blue channel" and "red channel" respectively. A summary of the absorption and emission wavelengths can be found in Table 3.1.

	F_2^{2+}(2Mg)-center	F_2^{+}(2Mg)-center
λ_{ex}	435 nm	620 nm, 335 nm
λ_{em}	520 nm	750 nm
	"blue" negative Type I	"red" positive Type II

Table 3.1.: Summary of excitation and emission wavelengths for the color centers used within this study.

3.2. The Zeiss LSM 710 ConfoCor 3

For the readout process of the FNTD, the inverted design confocal laser scanning microscope LSM 710 ConfoCor 3 (Carl Zeiss Microscopy GmbH, Jena, Germany) is used together with the control software "ZEN 2009" (Zeiss), both provided by the Light Microscopy Facility at DKFZ (Fig. 3.4).

A detailed summary of the experimental procedure for a suitable 3D readout of FNTDs, important features of the LSM 710, as well as signal processing is published in [3]. Therefore only a brief introduction to the applied methods will be given here.

- Glass bottom microwell dishes (MatTek Corp., Ashland, MA, USA; Part No. P35G-1.5-20-C), coupled to the objective by immersion oil, are used to position the

FNTDs within the microscope. They are placed with their optical c-axis parallel to the polarization of the laser light and with their polished side facing down.

- The LSM 710 is equipped with various lasers [12] of which for this work only the 633 nm He-Ne-laser and the Ar-laser (458, 488 and 514 nm) were utilized. For every laser there are several parameters adjustable with the above mentioned software. The most important ones are the relative laser power p (in percent of the maximum absolute laser power), the time of the laser focus remaining on one position called dwell time τ, and the number of rescans R.

- There are different objectives built in the LSM 710. For all experiments carried out in this study the 63x oil objective was used.

- It is possible to choose different sizes of areas scanned by the laser and to vary the resolution *i.e.* the number of pixels for every frame size.

- The microscope holds two different detector systems. It is possible to choose between two photomultiplier tubes (PMT), one transmission PMT (T-PMT) and two avalanche photodiodes (APDs). For FNTD readout the APDs in photon counting mode have been used because of their enhanced near infrared sensitivity compared to PMTs. The photon counting rate is limited to $\eta_{max} = 20\,\mathrm{MHz}$ in order to avoid damage.

- Acquired images together with all relevant parameters are saved in the LSM5 format. These files can be imported by other software for further analysis.

- It has been shown that the best signal is obtained in a depth of $30\,\mu\mathrm{m}$. If not mentioned otherwise, it was always focused in this depth for readout.

3.3. Data Processing

3.3.1. Software

ImageJ

Image stacks were analyzed with ImageJ, a Java-based public domain software developed by Wayne Rasband [13] together with the plugin 'Mosaic' developed by the 'MOSAIC' group at the Swiss Federal Institute of Technology Zurich (ETH). Results were exported to Excel files, which for their part were imported in "R" as data frames.

R

Data processing was generally done with "R". This is an open source software developed by Robert Gentleman and Ross Ihaka [14] and specialized on statistical computing and graphics. In previous works there have been developed a series of tools specialized to analyze LSM images by S. Greilich et al in the 'Heavy Ion Therapy' group at DKFZ. These

tools can be found in the 'FNTD' package. In the following only the most important ones shall briefly be mentioned:

- **LSM Reader.** Images are stored by the LSM710 in the .lsm format. The LSM reader, originally from Image J, was wrapped in the 'FNTD' package to be able to import .lsm-images directly into R.

- **Particle Tracker.** This tool by the 'Mosaic' group searches the image for bright spots (in our case particle tracks) and returns their positions on the image. A good description of the algorithm is given in [15].

- **Background Subtractor.** Also provided by the 'Mosaic' group this tool uses a histogram based algorithm to analyze an image towards its red background, *i.e.* the a priori transformed color centers. It returns an image of the background substituting signal with interpolated background values. For a detailed description, see also [15].

- **"track.moments"**. This command of the FNTD package summarizes and calculates values of interest of every single track found by the Particle Tracker, such as mean counts and minimum and maximum counts per track.

3.3.2. Fluorescence Signals

As a longer dwell time τ as well as more rescans R enhance the absolute number of photon counts N, it is convenient to introduce a normalized quantity which is independent of τ and R. This is done by defining the count rate η [3]:

$$\eta = \frac{N}{R\tau} \tag{3.5}$$

As results from red readout (p = 100%) have to be compared to results from blue readout (p $\approx$ 10%) the adjusted count rate becomes a quantity of interest, due to its independence of the laser power.

$$\eta_{adj} = \frac{\eta}{p} \tag{3.6}$$

Note that the unit of η and η_{adj} is "Hz".

When calculating the ratio of conversion of color centers during irradiation, it has to be considered, that in the blue channel the color center concentration diminishes whereas it increases in the red channel. Hence, with η' being the adj. count rate after irradiation and η_0 the adj. count rate before irradiation and further considering that $\eta' > \eta_0$ in the red channel and $\eta' < \eta_0$ in the blue channel, the signal obtained from irradiation is

$$\eta_{sig} = |\eta' - \eta_0| \,. \tag{3.7}$$

With the Signal η_{sig} and the unirradiated background η_0 a conversion ratio χ for blue and red images can be defined as

$$\chi := \frac{\eta_{sig}}{\eta_0} \tag{3.8}$$

3.3.3. Inversion of blue channel images

On blue channel images tracks appear as dark spots. But as the provided R routines for image analysis are made to work on bright spots obtained in the red channel, the negative image first has to be inverted and then processed with the common routines to obtain the track positions ("particle tracker") and the background ("get.background"). The inversion was made by

$$C_{inv}(x) = [-(C(x) - C_M)] + C_M \tag{3.9}$$

where C(x) are the counts at pixel x of the image and

$$C_M = \frac{\max(C(x)) + \min(C(x))}{2} \quad . \tag{3.10}$$

The background was inverted again using (3.9) becoming then the foreground (fg). The track positions were applied on the foreground and on the original image. For blue images the difference between the interpolated foreground and the minimum number of counts was regarded as the obtained signal.

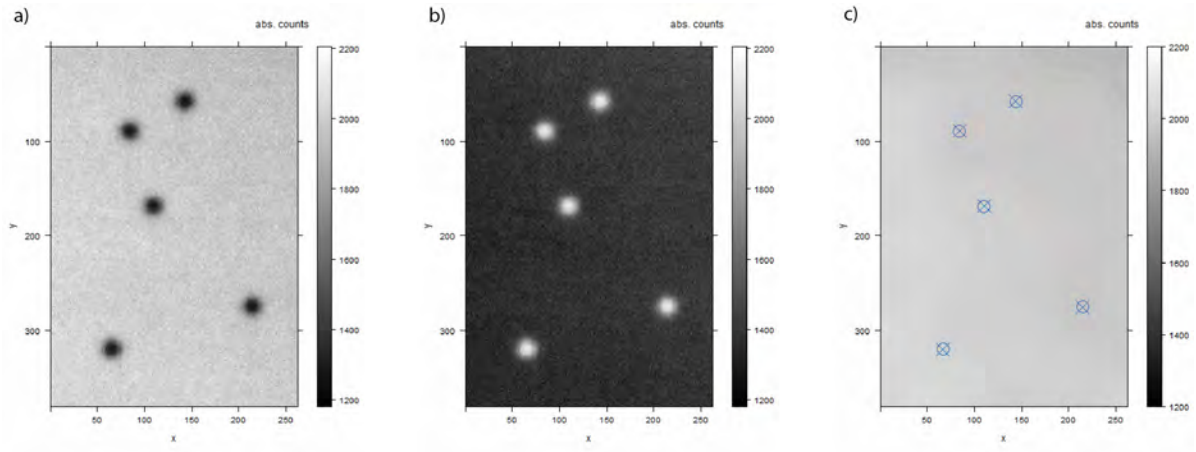

Figure 3.5.: Inversion applied on an image of Xe-tracks. a) Original blue channel image b) Inverse image c) Track positions applied to foreground image.

3.3.4. Increase of red signal after blue readout

In a previous work by S. Hoof [15] the transformation of color centers by 2PA processes when using the 458 nm Ar-laser line at the LSM 710 (see Sec. 3.1.3) was investigated.

Further investigation found a relative laser power p of maximum 10% to be suitable for most readouts without (1) inducing an important amount of color center transformations and (2) driving the APD into saturation [15].

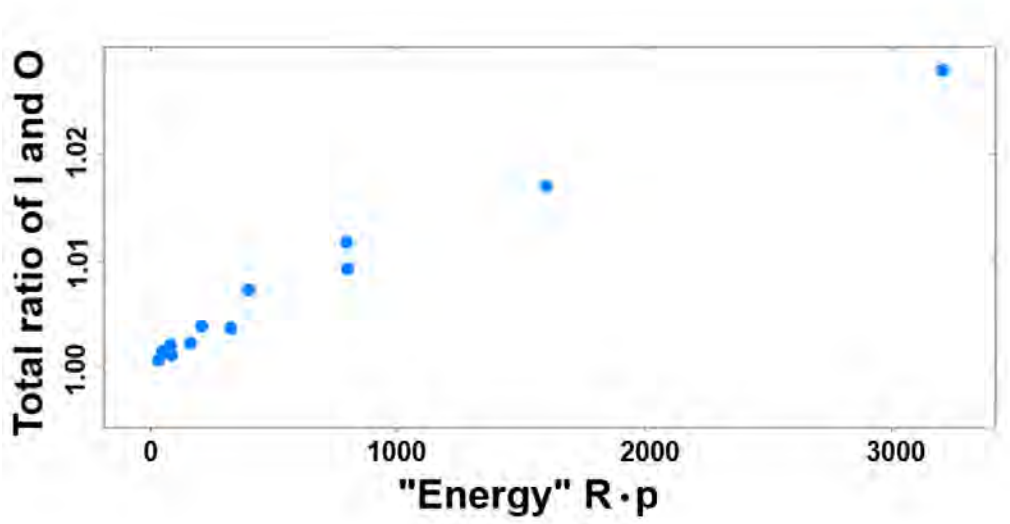

Figure 3.6.: Ratio of Background (O) and Signal (I) for different writing energies of the Ar-laser. The induced signal was measured with a dwell time $\tau = 177.317\,\mu$s immediately after irradiation with the blue laser. Reprinted from [15].

3.4. Ratio of a priori color center concentrations

In order to derive a correlation of the population of the F_2^{2+}(2Mg)-centers (C_{blue}) and of the F_2^{+}(2Mg)-centers (C_{red}) from measured fluorescence count rates, we use a simple model assuming:

- The total amount of color centers is constant
- Transformations occur only from blue to red color centers. Re-transformations are neglectable
- The adjusted count rates before (η and φ) and after (η' and φ') irradiation are directly proportional to the color center concentrations

$$\eta = \alpha \cdot C_{blue} \qquad \varphi = \beta \cdot C_{red} \tag{3.11}$$

The factors α and β are determined by external influences such as fluorescence yield, absolute laser power, the filters used by the microscope etc. and technically not quantifiable. But it is reasonable that $\alpha \neq \beta$. As α and β are unknown, the sum of adj.

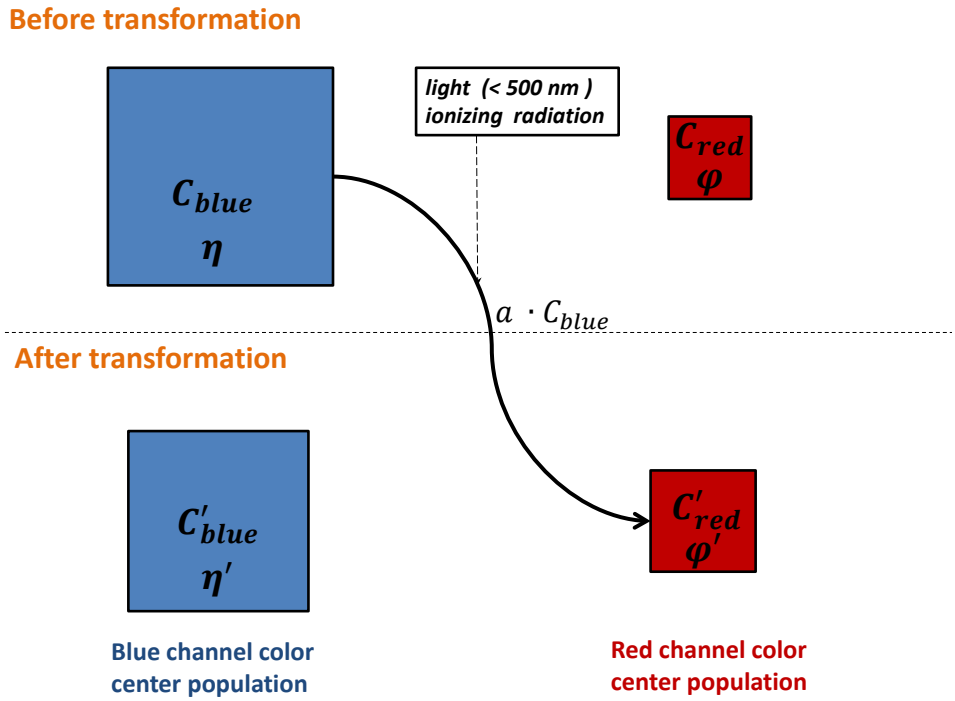

Figure 3.7.: Schematic change of color center concentrations in a transformation process.

count rates allows no conclusion about the total color center concentration. Therefore this model is limited to relative relations.

Fig. 3.7 illustrates how a transformation process causes that a fraction a of the amount of blue color centers (F_2^{2+}(2Mg)-centers) passes to the population of red color centers (F_2^{+}(2Mg)-centers). Therefore the concentrations of color centers after transformation are

$$C'_{blue} = C_{blue} - a \cdot C_{blue} \tag{3.12}$$

$$C'_{red} = C_{red} + a \cdot C_{blue} \tag{3.13}$$

Eq. 3.12 yields

$$a = 1 - \frac{C'_{blue}}{C_{blue}} \overset{3.11}{=} 1 - \frac{\eta'}{\eta} \tag{3.14}$$

Dividing Eq. 3.13 by C_{red} and further substituting with 3.14 and 3.11 leads to

$$\frac{C'_{red}}{C_{red}} = 1 + a \cdot \frac{C_{blue}}{C_{red}}$$

$$\frac{\varphi'}{\varphi} - 1 = \left(1 - \frac{\eta'}{\eta}\right) \cdot \frac{C_{blue}}{C_{red}}$$

$$\frac{C_{red}}{C_{blue}} = \frac{\left(1 - \frac{\eta'}{\eta}\right)}{\left(\frac{\varphi'}{\varphi} - 1\right)} \overset{3.7}{=} \left(\frac{\eta_{sig}}{\eta}\right)\left(\frac{\varphi_{sig}}{\varphi}\right)^{-1} \tag{3.15}$$

Considering the above definition of the conversion ratio 3.15 simplifies to

$$\frac{C_{red}}{C_{blue}} = \frac{\chi_{blue}}{\chi_{red}} =: \Gamma \tag{3.16}$$

Thus, by determining the conversion ratios for both channels it is possible to estimate the ratio of the a priori color center concentration. Calculation of the absolute values is however impossible due to the unknown factors α and β in Eq. 3.11. Γ should be independent of does, but best predicted from high dose signals, *i.e.* signals with small errors.

3.5. Irradiation

3.5.1. Photon irradiation

For irradiation with X-rays a Siemens Artiste linear accelerator (LINAC) was utilized, which is in use at DKFZ for research purposes only. The linac provides a flattening-filter free high dose-rate beam (2000 MU/min) at 7 MV.

3.5.2. Irradiation with HCPs

The irradiation with HCPs was made at the Heidelberger Ion-Beam Therapy Center (HIT). Belonging to the Heidelberg University Hospital, in this clinical radiotherapy facility patients are treated with protons and carbon ions. Particles are accelerated by a combination of a linear accelerator and a synchrotron and are delivered to patients in three treatment rooms of which one is equipped with the world's first carbon ion gantry, whereas the other ones have horizontal beam lines. Additionally, there is a fourth beam line for research and quality assurance in a separate room. For beam delivery an active scanning technique is used, applying intensity-modulated raster scanning pencil beams on virtual tumor slices.

3.6. Absorption measurements

A photospectrometer, PerkinElmer's VICTOR3 multilabel counter model 1420 well plate reader, was used to measure optical absorption FNTDs. After Eq. 2.4 this absorption is correlated to the color center concentration. To address F_2^{2+}(2Mg)-centers the photospectrometer measured an absorbance of 450 nm. In order to be able to analyze the FNTDs, it was necessary to build a PVC-well-plate-dummy of a Falcon Multiwell™ 3047 24 well plate with drill holes on which the FNTDs were mounted as shown in Fig. 3.8.

Figure 3.8.: Setup for Photospectrometry. Wellplate-Dummy built after a Falcon Multiwell™ 3047 24 well plate with FNTDs fixed on its surface above the drill holes.

Additionally to the 20 detector holes, two blank holes and two black holes were left on the dummy for reference measurements. The holes on the upper right side of the dummy were chosen as blanks because in a zero measurement these two holes have shown a systematically higher absorption. In addition three measurements were made with a completely empty well-plate-dummy in order to normalize the measurements.

4. Experiments

4.1. Basic Characteristics of Emission

4.1.1. Laser power and stability

A long time stable laser power is fundamental for reproducible multiple readouts. To analyze laser stability an experiment was carried out [N. Schudell, pers. comm.], measuring the absolute laser power of the Ar-Laser off focus with the power meter Ophir Photonics Nova II over 100 minutes. The power meter was located on the object table and read out automatically every 0.064 s by the power meter software (StartLab 2.4.0).

4.1.2. Dependence of adjusted count rate on dwell time and laser power

This experiments aim was to analyze the applicability of the concept "adjusted count rate" (Eq. 3.6) to the blue signal, *i.e.* independence from dwell time and laser power. For this purpose an unirradiated FNTD (FNTD ID: tr1000) was read out multiple times in the same area of 67.48 μm $\times$ 67.48 μm at a depth of 30 μm and with 256 pix $\times$ 256 pix in the blue channel. The readout was repeated with all possible combinations of relative laser power and dwell time given in Table 4.1. To avoid saturation of the APD, a 50/50 beam splitter was introduced into the light path in front of the ADP.

Dwell time [μs]	177.32	100.85	50.42	25.21	12.61	6.3	5.09	3.15	2.55	2.00
Relative laser power [%]	100	70	50	30	10	3	1	0.3	0.2	0

Table 4.1.: Laser and dwell time settings used.

4.2. Photochromatic transformations

4.2.1. Depletion of blue signal

This experiment observed the change of the blue signal during readout due to photochromatic transformation. An unirradiated FNTD (FNTD ID: tr1002) was read out 80 times

continuously on the same area, *i.e.* without any time delay between two images (time series). To optimize total experiment time, the scanned area was of $30\,\mu\text{m} \times 30\,\mu\text{m}$ with a dwell time fixed to $177.317\,\mu\text{s}$. The mean count rate per entire image was evaluated. This procedure was applied in all following time series (Sec. 4.2.2- 4.2.4).
To check dependence of the depletion on laser power the time series were taken with 10% and 3% laser power. Higher laser powers were not possible due to saturation of the APD.

4.2.2. Red signal stability after 2PA

In an approach similar to S. Hoof [15], the blue time series were followed immediately by a red channel readout with 100 % laser power, to observe the signal induced by 2PA. However, as in the experiments in 4.2.1 an unexpected decrease of the red signal was seen, a time series of 80 images was taken instead of a single image. For this, the scanned area was of $45\,\mu\text{m} \times 45\,\mu\text{m}$ with the same dwell time as for the blue series. The larger area of the red images allows obtaining a background signal outside of the image part [15], which was not in contact with the blue laser. The experiment was repeated with 30% laser power to assess the influence of the laser power on the signal dynamic.

4.2.3. Interrupted readout of red signal after 2PA

To discriminate the influence on red signal depletion by laser vs. thermal effects, a red time series similar to 4.2.2 was measured after inducing a signal by 2PA. However, here the laser was switched off and on in regular intervals of 10 images during a time series of 80 images in total.

4.2.4. Red signal stability after photon irradiation

To study if the red signal induced by ionizing radiation exhibits a similar decrease as after 2PA, we read out an FNTD with the same method as in 4.2.2 immediately after irradiation with X-rays. Here a longer time series of 200 images was made. A dose of 100 Gy ($\pm$10%) delivered by the research LINAC at DKFZ was applied and readout started about 5 min. after irradiation with 1% laser power.

4.2.5. Signal range and dose response

Photon-radiation

This experiment should yield the possible range of count rates to expect in the blue channel as well as its dose dependence. Also, the conversion ratio (Eq. 3.8) as function of dose was studied. 15 previously irradiated FNTDs [16] were analyzed by blue channel readout. This set of photon irradiated FNTDs (Table 4.2) had previously been analyzed for dose response in the red channel.

	FNTD ID	Dose [Gy]	Irradiation Facility
1	rm1000	0.00	LINAC, DKFZ
2	rm1001	0.01	LINAC, DKFZ
3	rm1002	0.03	LINAC, DKFZ
4	rm1003	0.1	LINAC, DKFZ
5	rm1004	0.3	LINAC, DKFZ
6	rm1005	1	LINAC, DKFZ
7	rm1006	3	LINAC, DKFZ
8	rm1007	10	LINAC, DKFZ
9	rm1008	30	LINAC, DKFZ
10	rm1009	100	LINAC, DKFZ
11	rm1010	300	LINAC, DKFZ
12	rm1011	100	γ-cell, Risø
13	rm1012	300	γ-cell, Risø
14	rm1013	1000	γ-cell, Risø
15	rm1014	3000	γ-cell, Risø
16	rm1015	10000	γ-cell, Risø

Table 4.2.: Irradiation Data. To obtain a wide dose range, the FNTDs were not only irradiated with a linear accelerator (LINAC) as used in radio therapy, but also with a high activity γ-cell at DTV Nutech (Risø), Denmark. The irradiations were made in July 2012 and the corresponding detectors response in the red channel can be found in [3].

Every blue and red channel readout was performed in a depth of 90 μm. For the images, the scanned area was of 135 μm $\times$ 135 μm scanned with a laser power of 10% and a pixel dwell time of 75.73 μs. The red readout was made with 100% laser power for doses until 1 Gy and for higher with 1%. Also, the pixel dwell time was lower for red images (53.78 μs) whereas the scanned area for the red laser was 225 μm $\times$ 225 μm, with the purpose to include an area not affected by the blue laser. For each image the mean pixel counts were calculated and then transformed into adjusted count rates after Eq. 3.6. Also the conversion ratio χ was calculated after Eq 3.8. The adj. count rates of rm1000 were assumed as background η_{bg} and $\eta_{sig} = \eta_{bg} - \eta_i$.

Ion radiation (Xe ions)

To study the conversion ratio in the case of ions, we chose the detector rh11 for readout in the blue channel as it has large tracks where full saturation can be assumed. Also, there are expected to show only small average effects due to the point spread function. This FNTD had been irradiated with $5.16 \cdot 10^5$ Xenon particles per cm^2 with an energy of 5.87 MeV/u at RADEF, Finland for a previous study [17]. In order to obtain a good signal to noise ratio (SNR) in reasonable time from the particle tracks, a small area of 13.01 μm $\times$ 18.90 μm was scanned with a high repetition rate (rescans R = 8), a maximum dwell time (τ = 177.317 μs) and a relative laser power of 10%. The background count

rate by the background subtractor plugin and the minimum count rate were evaluated per track. The conversion ratio χ was calculated using Eq. 3.8.

4.3. Correlation Experiments

4.3.1. Coloration and blue signal

As the untransformed color centers were suspected to be in relation to the color of the detector, the correlation of the optical absorption at 450 nm and the blue signal had been of particular interest. For 20 FNTDs, provided by J.Bartz, Landauer Inc., covering the range of yellow-greenish coloration found during the crystal growth process, the coloration was quantified using optical absorption by photospectrometry. The well-plate-dummy as described in chapter 3 with the two blank holes and the two black holes was inserted in the well plate reader. The absorption was measured 10 times per position. Mean values were obtained by averaging 10 measurements of the well-plate-dummy. The standard deviation and the standard error of the mean value were calculated for each measurement. Mean values were normalized with the blank measurements (*i.e.* without samples on the well plate) to account for effects (shadowing, etc.) of the dummy.

$$\text{Norm} = \frac{\text{Mean}}{\text{Mean Blank}}$$

For comparison with the count rates it was always used this normalized value.

4.3.2. Intrasample variation of blue signal

The unirradiated detectors used in Sec. 4.3.1 were analyzed for red and blue count rates in two defined areas as seen in Fig. 4.1. Images were taken in 30 μm depth of an area of 135 μm $\times$ 135 μm. Relative laser powers were chosen 10% for 458 nm and 100% for 633 nm. Red images were read out for later comparison with irradiated samples.

4.3.3. Blue signal before and after irradiation

In order to gain information about the blue signals after irradiation the same set of FNTDs was irradiated homogeneously and read out in the same areas as in Sec. 4.3.2. By comparison of the signals before and after irradiation it should be assessed the possibility to deduce the unirradiated blue signal by a single readout of the irradiated signal.

Irradiation

Irradiation happened partly with photons at the DKFZ research LINAC and partly with $3 \cdot 10^6$ 1/cm^2 carbon ions at HIT. A detailed overview is given in Table 4.3 and the experimental setups are shown on Fig. 4.2 and 4.3. All FNTDs were irradiated perpendicularly to their surface. For dose build-up the detectors in the LINAC were covered

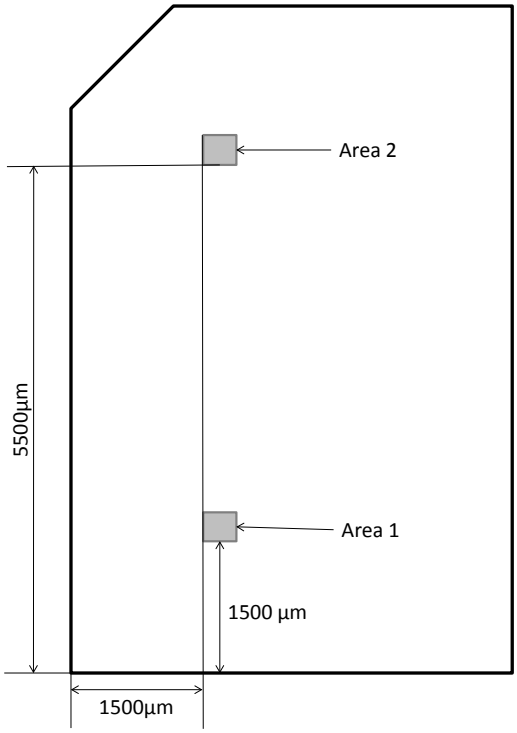

Figure 4.1.: Scanned areas of the set of 20 FNTDs.

with 2 cm RW 3. In order to get an equal dose in all FNTDs they were positioned in a circle around the isocenter.
Irradiation at HIT was carried out in the beam entrance channel. For stability the FNTDs were stuck to a PMMA-block. The homogeneous field had the size of $5\,\mathrm{cm} \times 5\,\mathrm{cm}$, so the detectors were positioned in this area around the isocenter.

FNTD	Radiation	Facility	Energy
01	Photon	LINAC, DKFZ	100 Gy
02	12C	HIT	91.13 MeV/u
03	12C	HIT	91.13 MeV/u
04	Photon	LINAC, DKFZ	100 Gy
05	12C	HIT	91.13 MeV/u
06	Photon	LINAC, DKFZ	100 Gy
07	Photon	LINAC, DKFZ	100 Gy
08	Photon	LINAC, DKFZ	100 Gy
09	12C	HIT	91.13 MeV/u
10	Photon	LINAC, DKFZ	100 Gy
11	12C	HIT	91.13 MeV/u
12	Photon	LINAC, DKFZ	100 Gy
13	12C	HIT	91.13 MeV/u
14	Photon	LINAC, DKFZ	100 Gy
15	12C	HIT	91.13 MeV/u
16	Photon	LINAC, DKFZ	100 Gy
17	12C	HIT	91.13 MeV/u
18	Photon	LINAC, DKFZ	100 Gy
19	12C	HIT	91.13 MeV/u
20	Photon	LINAC, DKFZ	100 Gy

Table 4.3.: Irradiation data of 20 FNTDs

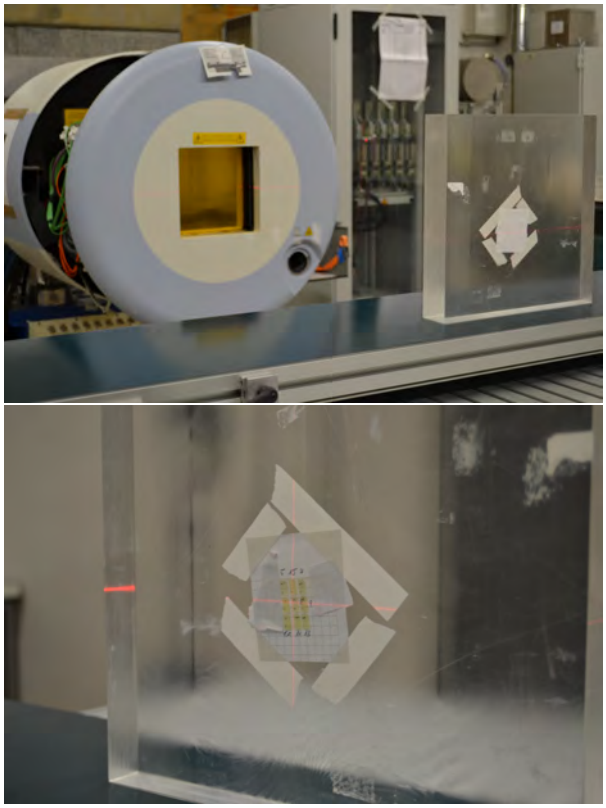

Figure 4.2.: Irradiation setup at HIT. Irradiation beam line with FNTDs glued to a PMMA-block and positioned in the isocenter.

Figure 4.3.: Irradiation setup at DKFZ. FNTDs positioned in a circle around the isocenter.

Irradiated FNTDs

The irradiated FNDTs were read out again at the same areas and with the same parameters as before irradiation, except that the relative power of the red laser was reduced to 10% for all photon irradiated FNTDs in order to avoid APD saturation.
Red and blue images of photon irradiated FNTDs were averaged and the mean value converted into adj. count rates. Images of FNTDs irradiated with carbon were processed in R with the background subtractor, particle tracker and "track.moments" to obtain the mean counts per tracks. This procedure worked out only for red images as tracks were not visible in the blue image. Hence, the particle positions found by the particle tracker were transferred form the red to the blue image. The blue adj. count rate was then obtained by averaging over the mean count rates calculated by the "track.moments"-tool at the track positions on the blue image. The evaluated mean adj. count rates were plotted against the normalized absorption as determined previously.

4.3.4. Intrasample red and blue signal correlation

First, an unirradiated FNTD (FNTD ID: tr1000) was read out in both the red and the blue channel within a depth of 30 μm. Single images were made on the 15 positions marked in Fig. 4.4. For best image quality the size of the readout area was set to 134.7 μm $\times$ 134.7 μm which were 1364 pix $\times$ 1364 pix for blue images. However, in a red image this correspond to 1152 pix $\times$ 1152 pix. Also dwell times depended on the readout channel and were chosen 75.73 μs for blue images and 22.41 μs for red images.

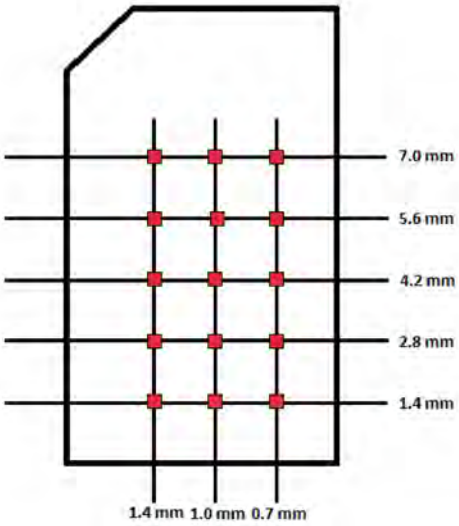

Figure 4.4.: 15 readout positions were used to compare red and blue signal intensities.

4.3.5. Sensitivity vs. blue signal

Using the obtained data of the set of 20 FNTDs, we assessed the feasibility of employing the blue signal to normalize the red signal variability. Therefore the red signal, *i.e.* $\eta_{sig} = \eta' - \eta_0$, measured after irradiation was plotted against the blue adj. count rates. This is a possibility to estimate the influence of the color center concentration on the signal strength.

Photons

To gain a value of the red signal for the photon irradiated detectors, the mean adj. count rate per image before irradiation was regarded as background and subtracted from the corresponding value after irradiation.

Ions

For ions the background count rates were calculated with the background subtractor. Then the red signal was determined trackwise by subtracting the interpolated background from the maximum adj. count rate within a track. All track signals per image were averaged yielding a mean adj. count rate per readout area. In order to assess whether also local normalization is possible within a single image, the red signal was correlated track by track to the blue adj. count rates for both read out areas.

4.3.6. Red background vs. blue signal

Photons

After an FNTD was irradiated with photons, there is no way to assess the previous red background of the unirradiated sample. For dosimetry it is thus of great interest if it is possible to deduce the red background from the blue signal after irradiation with an additional measurement in the blue channel. To approach this problem, both quantities were plotted against each other, using the same data as in the previous sections.

Ions

For ions the above mentioned interpolated background was used for correlation. This was regarded as test case since for tracks it is not necessary to estimate the background via the blue channel as the background subtractor provides a reliable algorithm for that.

5. Results

5.1. Basic Characteristics of Emission

5.1.1. Laser power and stability

The power measurements have shown a power of approx. 77 μW at sample with some variation of amplitude around 2.7% after a stabilization time of 40 min (2400 s). [N. Schudell, pers. comm.].

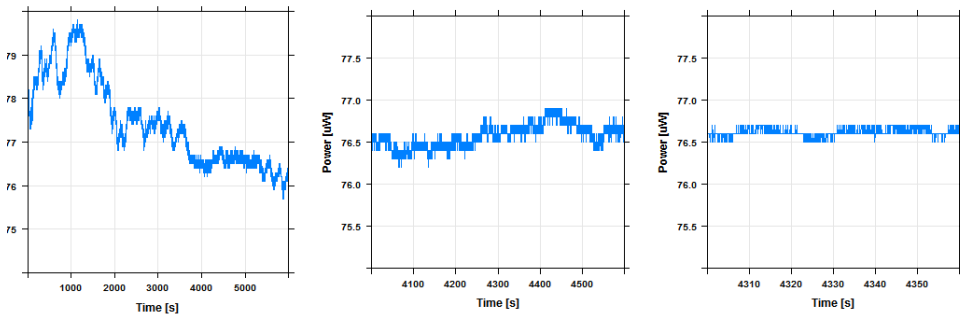

Figure 5.1.: Power variability of the 458 nm Ar-laser over Time (6000 s, 600 s and 60 s). [N. Schudell, pers. comm.]

5.1.2. Dependence of adjusted count rate on dwell time and laser power

Fig. 5.2 shows the compilation of adj. count rates as function of dwell time and laser power. The expected result for an independent adjusted count rate was a horizontal line. However, the graph drifts to higher adj. count rates for low laser powers. This is not due to non-linearities but to the APDs dark current and to ambient light. These are constant values (around 3.5 kHz) and have therefore a stronger impact for low laser powers [S.Greilich, pers. comm.].

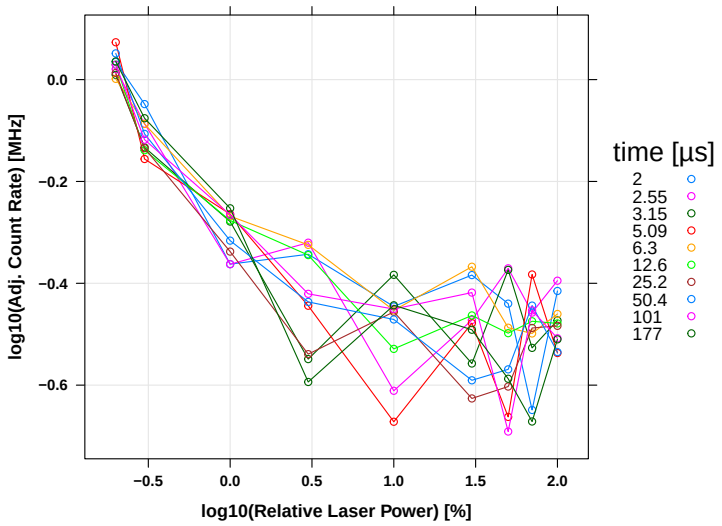

Figure 5.2.: Double logarithmical plot of count rates depending on laser power and dwell times.

5.2. Photochromatic transformation

5.2.1. Depletion of blue Signal

The results are displayed in Fig. 5.3 and show how the 10% signal decreases in time as the 2PA-process transforms color centers. After 80 continuous readouts roughly corresponding to an "energy R·p" of 800 a.u. at $\tau = 177.317\,\mu$s (see Fig. 3.6) the adjusted count rate diminished less than 1%.

5.2.2. Red Signal Stability after 2PA

Reading out the red channel immediately after inducing color center transformations and observing the signal devolution in time showed that the red fluorescence signal decreases and converges to a constant value. Results are depicted in Fig. 5.4. It can be observed that the signal read out with 100% laser power reaches a constant value. However, the signal read out with only 30% keeps decreasing. It seems that for the lower laser power the constant value has not been reached yet.

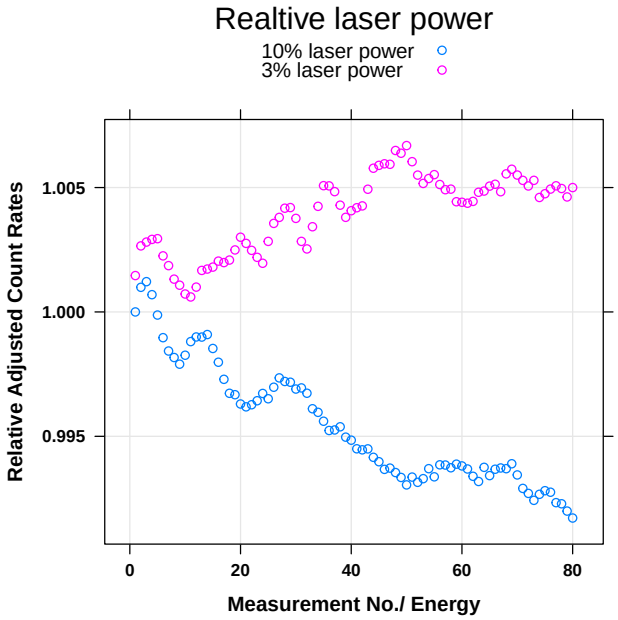

Figure 5.3.: Blue Signal Time curve for two different laser powers depending the number of measurements which is proportional to the "energy" $R \cdot p$ deposited in the sample (at $\tau = 177.317\,\mu$s).

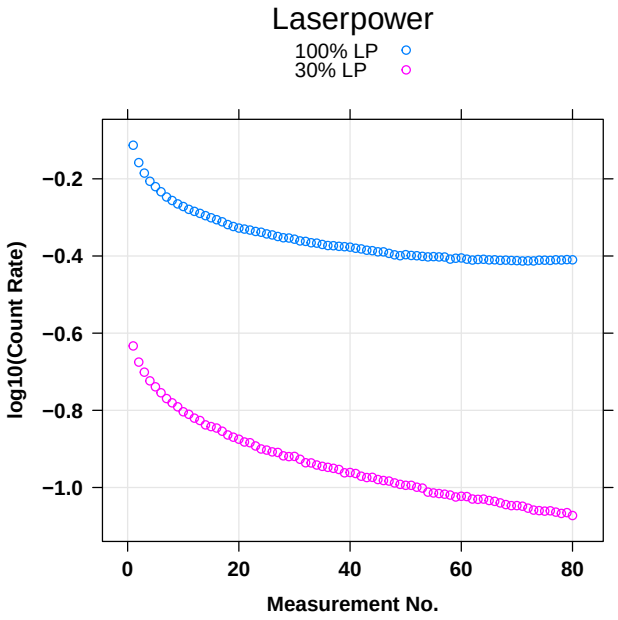

Figure 5.4.: Logarithmical red count rates after transformation induced by 458 nm Ar-laser light for different relative read-out laser powers depending on "energy" ($R \cdot p$ at $\tau = 177.317\,\mu$s).

5.2.3. Interrupted readout of red signal after 2PA

Shutting of the laser during a red readout time series yields Fig. 5.5. The signal seems to decrease exponentially. It stands out, that count rates before and after interruption almost coincide. The total signal decrease is of around 50% and it appears to keep decreasing.

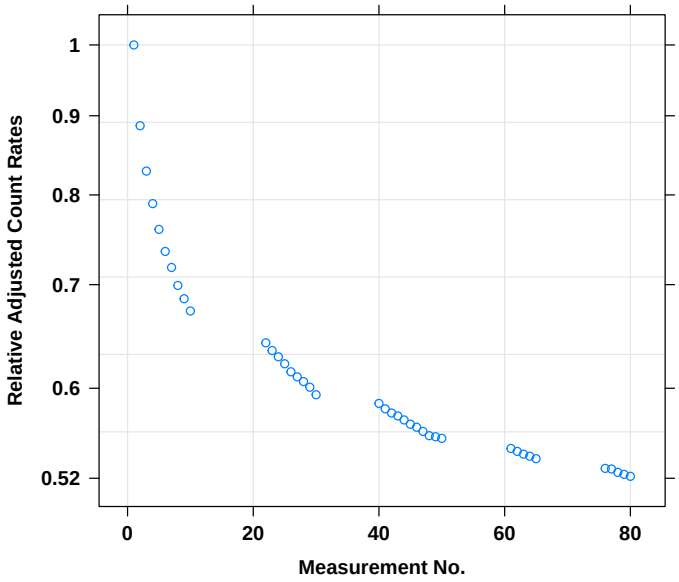

Figure 5.5.: Temporal evolution of red signal with interrupted readout laser. The Measurement No. corresponds to a deposited "energy" ($R{\cdot}p$ at $\tau = 177.317\,\mu$s).

5.2.4. Red signal stability after photon irradiation.

Fig.5.6 shows the red signal from five minutes on after irradiation delivering 100 Gy to the detector. It can be observed a fast signal increase of about 8% before the signal starts to diminish slowly.

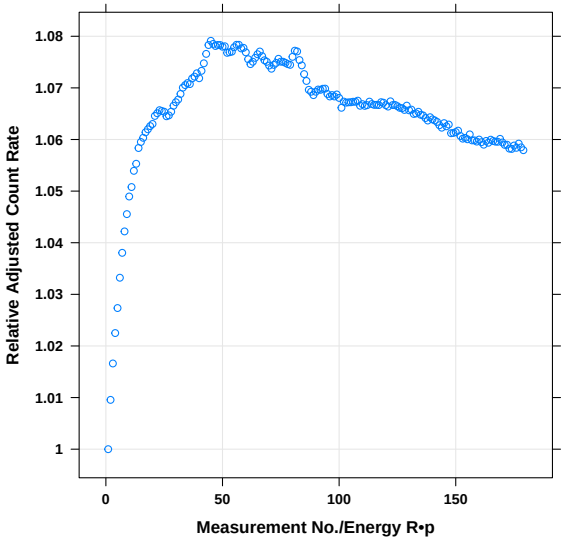

Figure 5.6.: Time curve of the measured Red Signal immediately after irradiation as function of deposited "energy" ($R \cdot p$ at $\tau = 177.317\,\mu$s).

5.2.5. Signal range and dose response

Photon-radiation

The results are summed up in Table 5.1 for the blue channel and in Table 5.2 for the red channel showing the mean number of counts per dose, the adjusted count rates and the conversion ratios χ_{blue} and χ_{red}. The standard deviation of the adj. count rates was assumed as good measure for their error. Errors of χ_{blue}, χ_{red} and Γ were calculated with the common propagation of error and can be found in Tab 5.4. Adjusted count rates were plotted double logarithmically against the dose, forming the photon response curves which are illustrated in Fig. 5.7. The blue channel curve exhibits a plateau at high count rates for doses lower than 10 Gy and decreasing count rates for higher doses. Concerning the FNTDs irradiated with the gamma-cell it stands out that count rates seem systematically higher. Furthermore the values for 300 Gy and 1000 Gy seem to suggest an increase. In contrast the red response increases with dose and shows a plateau for high doses. Here also the gamma-cell irradiated detectors yield systematically higher count rates.
The results show that blue adj. count rates range from 6 MHz to 40 MHz, whereas red adj. count rates range from 0.5 MHz to 360 MHz. The calculated conversion ratios are plotted against the dose (see Fig. 5.8). As estimated the ratio is constant for low does and increases with higher doses. The ratio of a priori color center concentrations Γ was calculated after Eq. 3.16 and plotted against dose (see Fig. 5.9). For high doses the graph seems to converge to $\Gamma = 0.003$, meaning that before irradiation the concentration of red centers is about 0.3% of the concentration of blue color centers.

FNTD ID	Dose [Gy]	Irradiated with	Mean Counts	Adj. Count Rate [MHz]	χ_{blue}
rm1000	0.00	LINAC	300.685	39.704	0.000
rm1001	0.01	LINAC	278.170	36.731	0.075
rm1002	0.03	LINAC	281.482	37.169	0.064
rm1003	0.1	LINAC	333.107	43.986	-0.108
rm1004	0.3	LINAC	301.465	39.807	-0.003
rm1005	1	LINAC	284.863	37.615	0.053
rm1006	3	LINAC	286.912	37.886	0.046
rm1007	10	LINAC	204.094	26.950	0.321
rm1008	30	LINAC	157.967	20.859	0.475
rm1009	100	LINAC	84.983	11.222	0.717
rm1010	300	LINAC	51.872	6.850	0.827
rm1011	100	Gamma-Cell	123.145	16.261	0.590
rm1012	300	Gamma-Cell	131.127	17.315	0.564
rm1013	1000	Gamma-Cell	134.290	17.732	0.553
rm1014	3000	Gamma-Cell	89.836	11.863	0.701
rm1015	10000	Gamma-Cell	72.144	9.526	0.760

Table 5.1.: Results of measurements in the blue channel with photon-irradiated FNTDs.

FNTD ID	Dose [Gy]	Irradiated with	Mean Counts	Adj. Count Rate [MHz]	χ_{red}
rm1000	0.00	LINAC	75.142	1.397	0.000
rm1001	0.01	LINAC	59.023	1.097	-0.215
rm1002	0.03	LINAC	37.600	0.699	-0.500
rm1003	0.1	LINAC	123.740	2.301	0.647
rm1004	0.3	LINAC	145.138	2.698	0.932
rm1005	1	LINAC	220.773	4.105	1.938
rm1006	3	LINAC	10.274	19.102	12.673
rm1007	10	LINAC	17.579	32.684	22.395
rm1008	30	LINAC	48.609	90.375	63.689
rm1009	100	LINAC	86.983	161.720	114.757
rm1010	300	LINAC	94.064	174.887	125.181
rm1011	100	Gamma-Cell	112.681	209.499	148.957
rm1012	300	Gamma-Cell	173.910	323.338	230.441
rm1013	1000	Gamma-Cell	195.201	362.923	258.775
rm1014	3000	Gamma-Cell	154.804	287.815	205.014
rm1015	10000	Gamma-Cell	138.144	256.841	182.843

Table 5.2.: Results of measurements in the red channel with photon-irradiated FNTDs.

Dose [Gy]	χ_{red}	χ_{blue}	$\lvert\Gamma\rvert$	$\Delta\Gamma$
0.00	0.000	0.000	-	-
0.01	-0.215	0.075	3.49e-1	4.94e-1
0.03	-0.500	0.064	1.28e-1	1.60e-1
0.1	0.647	-0.108	1.67e-1	1.75e-1
0.3	0.932	-0.003	2.79e-3	8.83e-2
1	1.938	0.053	2.72e-2	4.51e-2
3	12.673	0.046	6.61e-3	6.44e-3
10	22.395	0.321	1.43e-2	5.47e-3
30	63.689	0.475	7.45e-3	1.99e-3
100	114.757	0.717	6.25e-3	1.47e-3
300	124.181	0.827	6.66e-3	1.45e-3
100	148.957	0.590	3.96e-3	9.25e-4
300	230.441	0.564	2.45e-3	5.38e-4
1000	258.775	0.553	2.14e-3	4.75e-4
3000	205.014	0.701	3.42e-3	7.35e-4
10000	182.843	0.760	4.16e-3	9.22e-4

Table 5.3.: Ratio Γ of a priori color center concentration calculated for different doses (with error $\Delta\Gamma$).

FNTD	η_{red} [MHz]	$\Delta\eta_{red}$ [MHz]	η_{blue} [MHz]	$\Delta\eta_{blue}$ [MHz]	$\Delta\chi_{red}$	$\Delta\chi_{blue}$
rm1000	1.397	0.225	39.704	2.311	0.228	0.082
rm1001	1.097	0.211	36.731	2.377	0.197	0.081
rm1002	0.699	0.147	37.169	2.227	0.133	0.078
rm1003	2.301	0.398	43.986	2.661	0.390	0.093
rm1004	2.698	0.421	39.807	2.301	0.433	0.082
rm1005	4.105	0.586	37.615	2.603	0.633	0.086
rm1006	19.102	6.498	37.886	2.255	5.147	0.079
rm1007	32.684	8.636	26.950	2.052	7.242	0.065
rm1008	90.375	15.991	20.859	1.709	15.487	0.053
rm1009	161.720	26.012	11.222	1.262	26.367	0.036
rm1010	174.887	24.332	6.850	0.987	26.663	0.027
rm1011	209.499	30.815	16.261	1.571	32.732	0.046
rm1012	323.338	39.728	17.312	1.551	46.923	0.047
rm1013	362.923	43.980	17.732	1.725	52.404	0.051
rm1014	287.815	37.481	11.863	1.282	42.704	0.037
rm1015	256.841	36.802	9.526	1.284	39.661	0.035

Table 5.4.: Standard deviations for the measured adj. count rates together with the calculated errors of the conversion ratios.

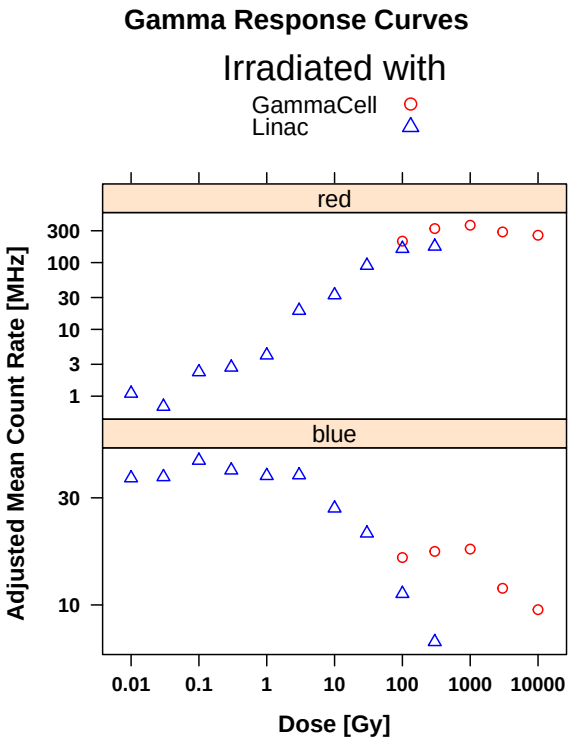

Figure 5.7.: Mean adjusted count rates for different doses in the both channels.

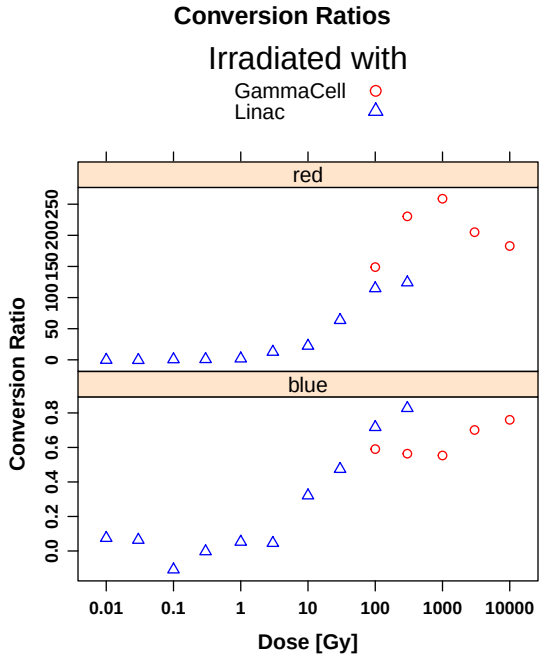

Figure 5.8.: Conversion ratios χ_{red} and χ_{blue} as a function of dose.

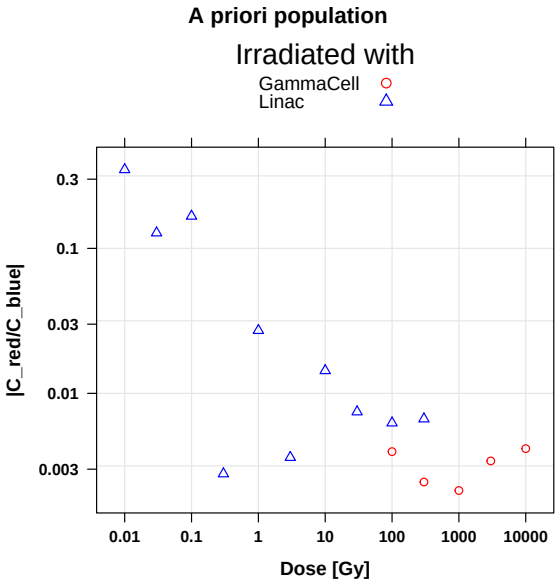

Figure 5.9.: Ratio of a priori color center concentration for detectors irradiated with different doses.

Ion radiation

The signal range was investigated for an ion irradiated FNTD. The results for every track are given in Table 5.5, which displays a conversion ratio χ for these tracks of about 40%. Count rates of obtained signals are around 5.5 MHz whereas the untransformed color centers yield a count rate of around 14 MHz.

track no	min counts	η_{min}^{adj} [MHz]	fg counts	η_{fg}^{adj} [MHz]	signal	η_{sig}^{adj} [MHz]	χ
1	1182.00	8.333	1977.03	13.937	795.03	5.604	0.4021
2	1191.00	8.396	1986.07	14.001	795.07	5.605	0.4003
3	1216.00	8.572	2005.61	14.139	789.61	5.566	0.3937
4	1209.00	8.523	1970.17	13.889	761.17	5.366	0.3864
5	1263.00	8.904	2018.24	14.228	755.24	5.324	0.3742

Table 5.5.: Results for Xenon-tracks in the Blue Channel.

5.3. Correlation Experiments

5.3.1. Coloration and blue signal

Absorption measurements

The results of the absorption measurements can be seen in Tab. 5.6. σ is the standard deviation of a measurement and $\frac{\sigma}{\sqrt{N}}$ is the standard error of the mean value.

Coloration vs. a priori blue signal

The mean count rate of the two blue images per detector obtained from the measurements of Sec. 4.3.2 plotted against the mean measured absorption normalized with the blank values shows a linear correlation of small slope (Fig. 5.10), *i.e.* that a great absorption variation translates into small count rate differences. Two high count rates (detectors 8 and 19) attract attention. They already had to be measured with a reduced laser power (1%) because of APD saturation when reading with 10% relative laser power. Another outstanding characteristic is represented by some lower count rates for low absorption coefficients (detectors 1 to 5 and 14). Not considering these artifacts, the result of this experiment is that the optical absorption is almost independent of the color center concentration, since concentration differences are small compared to absorption variations. However, the uncertainties of this measurement are too big to use the relation to estimate the blue signal from the detector absorption.

Poition	Well	FNTD Nr	Mean	σ	$\frac{\sigma}{\sqrt{N}}$	Mean Blank	Normalized
1	A01	1	0.907	0.0059	0.00133	0.148	6.120
2	A02	2	0.897	0.0048	0.00120	0.153	5.846
3	A03	3	0.945	0.0034	0.00076	0.165	5.714
4	A04	4	0.898	0.0043	0.00095	0.174	5.170
5	A05	black	3.874	0.0367	0.00775	3.819	1.015
6	A06	blank	0.194	0.0061	0.00137	0.198	0.978
7	B01	6	0.972	0.0024	0.00053	0.130	7.491
8	B02	7	0.983	0.0024	0.00053	0.134	7.319
9	B03	black	3.873	0.0326	0.00728	3.814	1.015
10	B04	8	1.032	0.0026	0.00058	0.161	6.402
11	B05	9	1.010	0.0034	0.00076	0.166	6.102
12	B06	blank	0.166	0.0053	0.00119	0.181	0.916
13	C01	10	0.978	0.0046	0.00103	0.131	7.476
14	C02	11	0.948	0.0065	0.00145	0.134	7.078
15	C03	12	0.896	0.0078	0.00174	0.152	5.907
16	C04	13	1.020	0.0078	0.00175	0.158	6.478
17	C05	14	0.987	0.0072	0.00162	0.162	6.081
18	C06	5	0.980	0.0074	0.00165	0.184	5.315
19	D01	15	0.957	0.0028	0.00064	0.124	7.689
20	D02	16	1.012	0.0027	0.00061	0.125	8.126
21	D03	17	0.973	0.0037	0.00082	0.142	6.832
22	D04	18	0.940	0.0042	0.00093	0.167	5.612
23	D05	19	1.041	0.0051	0.00114	0.163	6.388
24	D06	20	0.979	0.0055	0.00122	0.169	5.808

Table 5.6.: Results of optical absorption measurements of FNTDs.

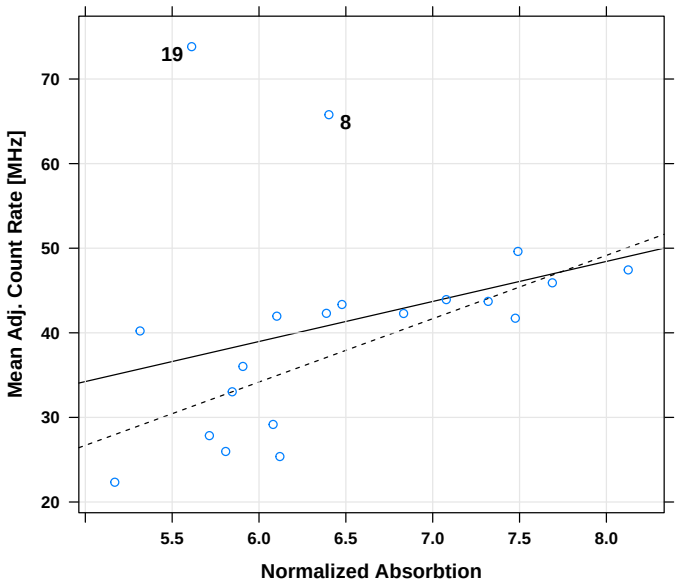

Figure 5.10.: Correlation of normalized optical absorption and mean adj. blue count rates. Dashed line: linear fit without detectors 8 and 19.

5.3.2. Intrasample variation of blue signal

In a first step the count rates obtained from the two measurements within the same detector were compared. Signals were averaged over all pixels of the images and plotted as seen in Fig. 5.11 (dashed line: slope 1). Numeric values for the areas 1 and 2 can be found in table of results in the appendix, together with the results for readout after irradiation. The plot yields a linear correlation of slope nearly 1 between the two read out areas. This means that the blue signal varies on a higher scale within the detector set than within the same sample. This is an important precondition for comparison of count rates and absorption of different FNTDs.

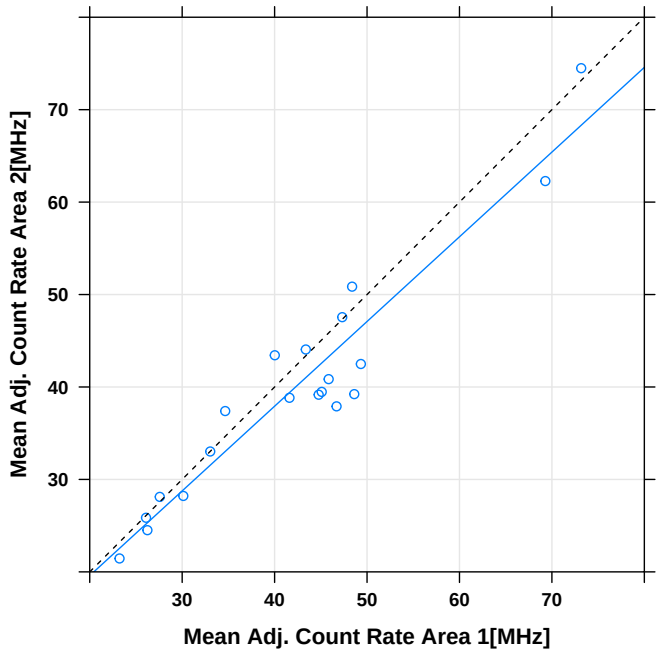

Figure 5.11.: Count rates of detector area 2 dependent on count rates of detector area 1. The dashed line represents the angle bisector.

5.3.3. Blue signal before and after irradiation

In order to get an overview of the measured adj. count rates per detector before and after irradiation, these values are represented in Fig. 5.13 and 5.14. The corresponding table can be found in the appendix (Tab. A.1). Furthermore minimum, maximum and mean adj. count rate were calculated for the 20 detectors (see Tab. 5.7. The adj. count rates of Table A.1 were used to calculate the blue and red conversion ratios for the photon irradiated FNTDs as well as the ratio of a priori color center concentration Γ (see Tab. 5.8). The results of the respective error calculation can be found in Tab 5.9.

The plot of the blue adj. count rates before and after irradiation yield a linear correlation for both kinds of radiation, photons and carbon ions. Hence, it is imaginable to deduce the a priori blue color center population from the irradiated detector by reading it out in the blue channel (see Fig. 5.12).

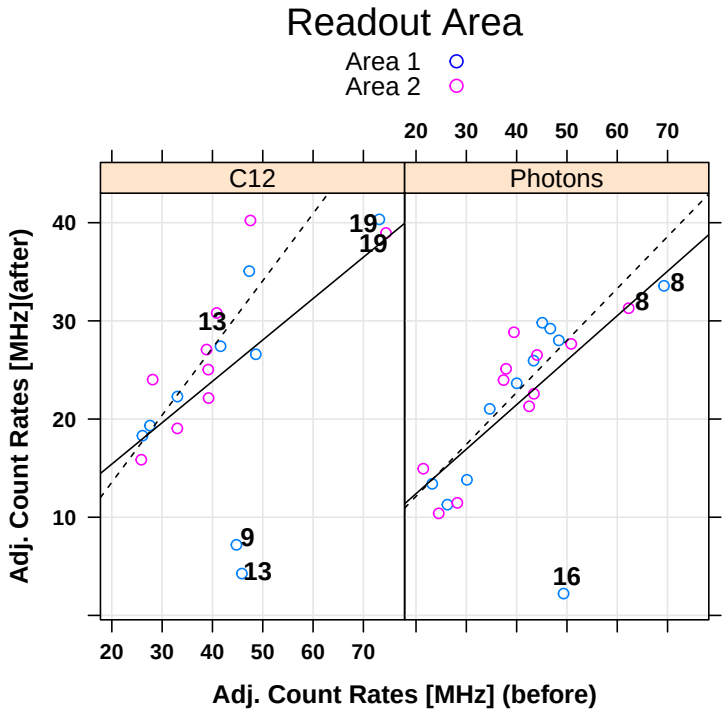

Figure 5.12.: Correlation of blue adjusted count rates before and after irradiation for the 20 measured detectors. Values are sorted by readout area and irradiation type. Dashed line: linear fit excluding detectors 9, 13, 16, 8 and 19.

Value	Max	Min	Mean	SD
Blue before [MHz]	74.486	21.449	37.900	8.617
Blue after [MHz]	40.338	2.221	21.550	8.432
Red Signal before [MHz]	2.022	0.109	0.764	0.596
Red Signal after [MHz]	21.862	0.485	9.467	8.425

Table 5.7.: Maximal, minimal and mean adj. count rates found in 20 FNTDs before and after irradiation with carbon and photons together with standard deviation (SD). For the calculation of the mean value and the SD detectors 8, 19 and 16 (area 1) were not considered since they have outstanding values.

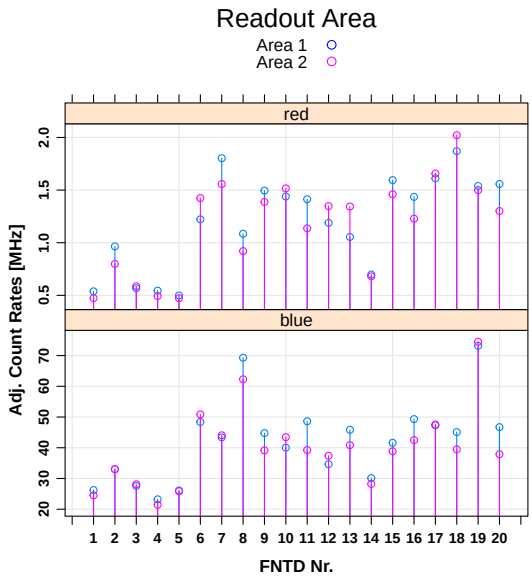

Figure 5.13.: Distribution of adj. count rates before irradiation in the red and blue channel.

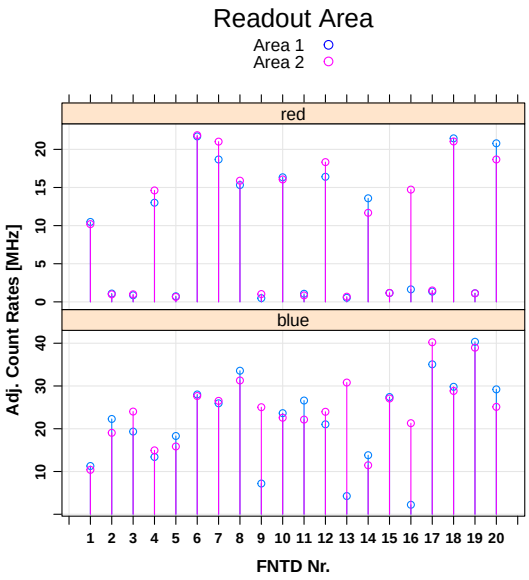

Figure 5.14.: Distribution of adj. count rates after irradiation in the red and blue channel.

	FNTD	χ_{red}	χ_{blue}	Γ
Area 1	1	19.474	0.430	0.031
	4	23.877	0.577	0.018
	6	17.757	0.579	0.025
	7	10.356	0.598	0.043
	8	14.121	0.484	0.039
	10	11.351	0.591	0.040
	12	13.799	0.607	0.031
	14	19.462	0.458	0.029
	[16]	[1.141]	[0.045]	[6.767]
	18	11.468	0.661	0.032
	20	13.347	0.625	0.030
Area 2	1	21.523	0.424	0.028
	4	29.607	0.697	0.011
	6	15.352	0.544	0.032
	7	13.491	0.602	0.032
	8	17.265	0.502	0.031
	10	10.593	0.520	0.050
	12	13.597	0.641	0.029
	14	17.153	0.406	0.037
	16	11.981	0.501	0.045
	18	10.405	0.731	0.029
	20	14.353	0.663	0.025
	Mean	15.730	0.564	0.032
	SD	4.937	0.092	0.009

Table 5.8.: Conversion ratios and ratio of a priori color center concentration for photon irradiated detectors. The area 1 value of detector 16 was excluded from averaging, since the FNTD was readout wrong.

FNTD	Area	$\Delta\eta'_{blue}$	$\Delta\eta'_{red}$	$\Delta\eta_{blue}$	$\Delta\eta_{red}$	$\Delta\chi_{red}$	$\Delta\chi_{blue}$	$\Delta\Gamma$
1		1.009	0.985	1.439	0.067	3.050	0.045	0.00565
4		1.894	2.210	1.787	0.073	5.156	0.093	0.00582
6		1.777	1.839	2.625	0.117	2.269	0.048	0.00446
7		1.341	1.441	2.159	0.146	1.160	0.043	0.00703
8		1.607	1.318	6.572	0.093	1.714	0.051	0.00646
10	1	2.137	1.516	2.555	0.135	1.497	0.065	0.00852
12		1.337	1.457	1.917	0.111	1.774	0.051	0.00584
14		1.191	1.071	1.513	0.078	2.660	0.046	0.00490
16		0.460	0.404	3.660	0.124	0.298	0.010	14.27944
18		1.696	1.878	2.345	0.158	1.395	0.051	0.00651
20		1.454	1.807	1.928	0.121	1.557	0.040	0.00504
1		1.061	0.859	1.596	0.064	3.442	0.051	0.00533
4		1.020	1.279	1.439	0.063	4.585	0.067	0.00288
6		1.470	1.644	1.934	0.120	1.730	0.036	0.00456
7		1.353	1.518	1.843	0.122	1.438	0.040	0.00485
8		1.798	1.208	6.156	0.085	2.066	0.057	0.00525
10	2	1.462	1.416	2.604	0.124	1.272	0.046	0.00818
12		2.052	1.350	2.919	0.148	1.795	0.074	0.00716
14		1.060	1.124	4.092	0.105	3.112	0.070	0.00830
16		1.684	1.509	3.124	0.119	1.687	0.054	0.00854
18		1.497	1.780	3.532	0.191	1.318	0.076	0.00898
20		1.333	1.387	1.867	0.115	1.657	0.048	0.00477

Table 5.9.: Standard deviation in MHz for the adj. count rates measured in the 11 photon irradiated detectors. Also, errors of conversion ratios $\Delta\chi_{blue}$ and $\Delta\chi_{red}$ as well as of the ratio of a priori color center concentration $\Delta\Gamma$.

5.3.4. Intrasample red and blue signal correlation

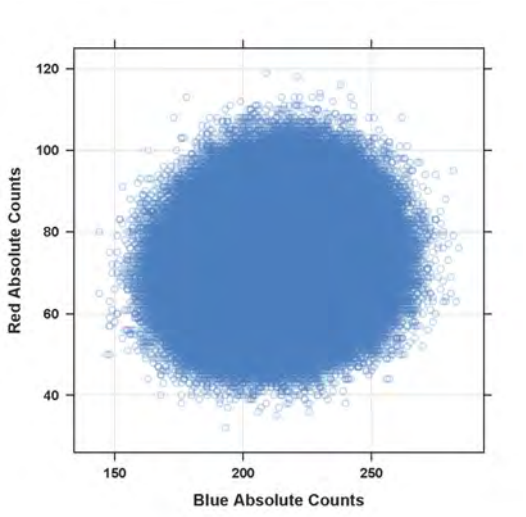

Figure 5.15.: Direct pixelwise correlation of red and blue counts within a single image.

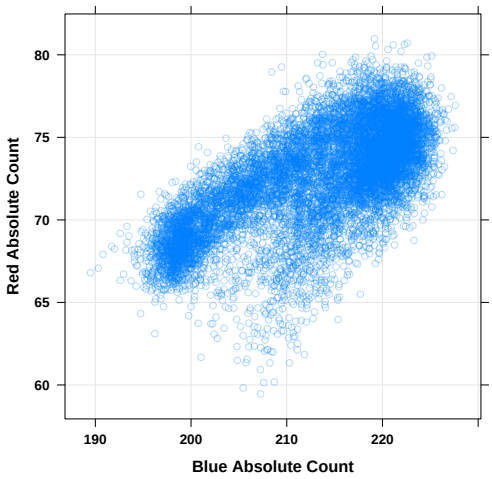

Figure 5.16.: Correlation of blue and red count rates within a single image with 10×10 pixels binned to one data point.

First, the correlation for every pixel within a single picture was analyzed. The pixelwise plot of the counts showed that the single pixel noise exceeds the correlation by far (Fig. 5.15). Thus, 10 pixels were binned to one data point to reduce noise. The result is shown in Fig. 5.16. Although there is still a significant spread, a linear correlation can be perceived such that high blue signals correspond to high red signals. In a next step of noise reduction not only one but all 15 images were taken into account for binning. Because of their different resolutions, in the analysis of the blue image, 561×561 pixels are binned to one data point whereas for the red image only 400×400 pixels form one data point. The result is plotted in Fig. 5.17 and yields a clear linear dependency of blue and red counts clarified by a linear fit. This correlation becomes even clearer when the mean counts of each of the 15 images (Fig. 5.18) is considered. By averaging over an entire image the fact that the high blue signal is associated with the high red signal has become more evident. The remaining spread of data points is due to crystal defects (Al-Al spinels). These defects cause image artifacts (shadows and dark spots), influencing the mean number of counts.

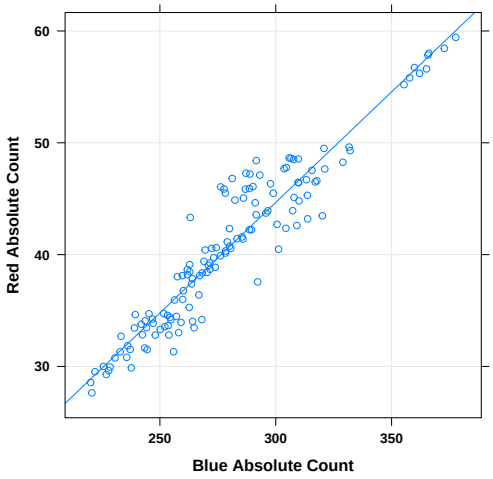

Figure 5.17.: Correlation within the area of 15 images with (561×561 and 400×400 pixel binned to one data point).

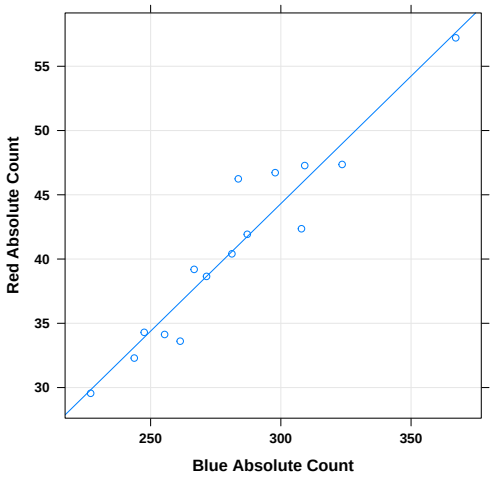

Figure 5.18.: Correlation of the red and blue mean count rates of 15 images.

5.3.5. Sensitivity vs. blue signal

Photons

For the photon irradiated FNTDs the red signal was plotted against the adj. count rates measured in the blue channel. As depicted in Fig. 5.19, the mean value of red signal in an image increases with the mean blue adj. count rates.

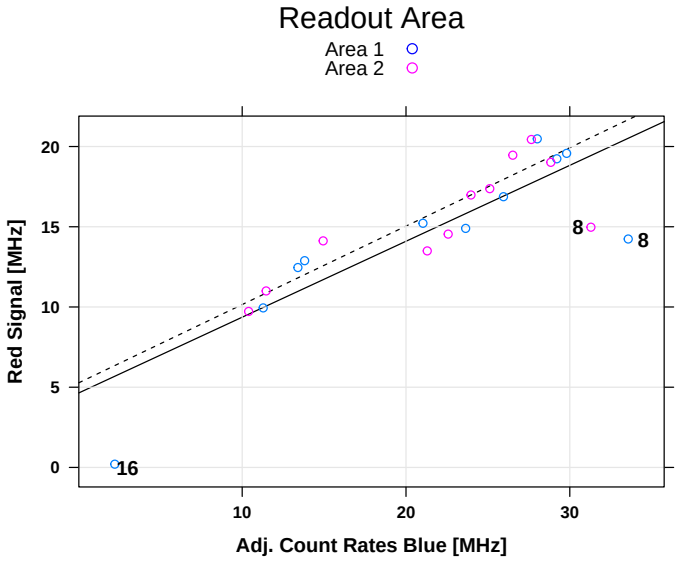

Figure 5.19.: Imagewise correlation between blue adj. count rates and red signal after irradiation with photons. Dashed line: linear fit without detectors 8 and 16.

Ions

The same observation as for photons can be done for the ion irradiated detectors. The results after averaging over all tracks found within an image are represented in Fig. 5.20. The graph shows a linear correlation between signal and blue adj. count rates. This confirms the result obtained for photons, meaning that it should be possible to normalize red signals of different detectors with their blue signal.
However, as seen in the track by track correlation (Fig. 5.21), this seems not to be feasible within a single image. Although it is here still possible to see the linearity of the mean track values, no tendency towards a correlation can be observed for tracks on a local scale. This is due to the same effect of high noise as in Sec. 5.3.4.

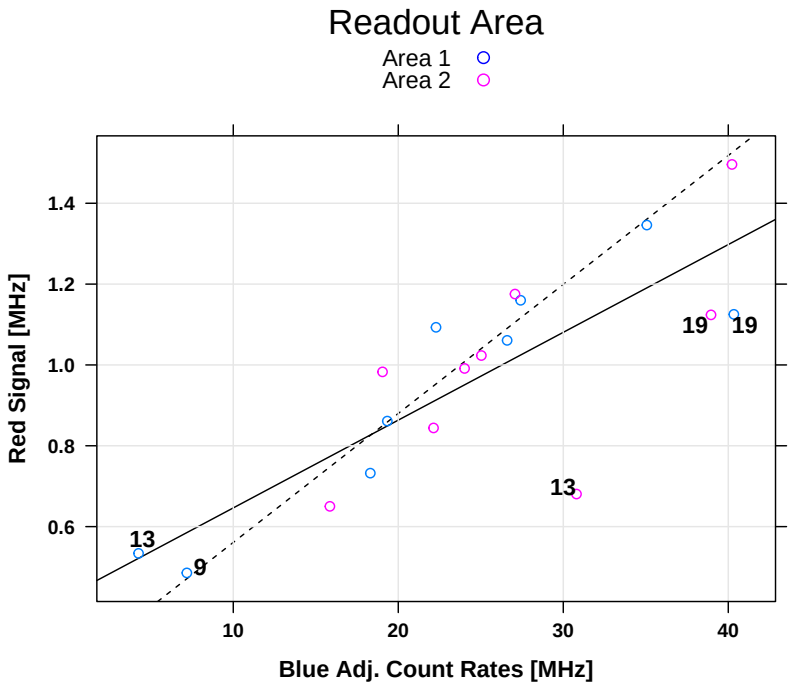

Figure 5.20.: Imagewise correlation of blue count rates and red signal for C12 irradiated detectors. Dashed line: linear fit without detectors 9, 13 and 19.

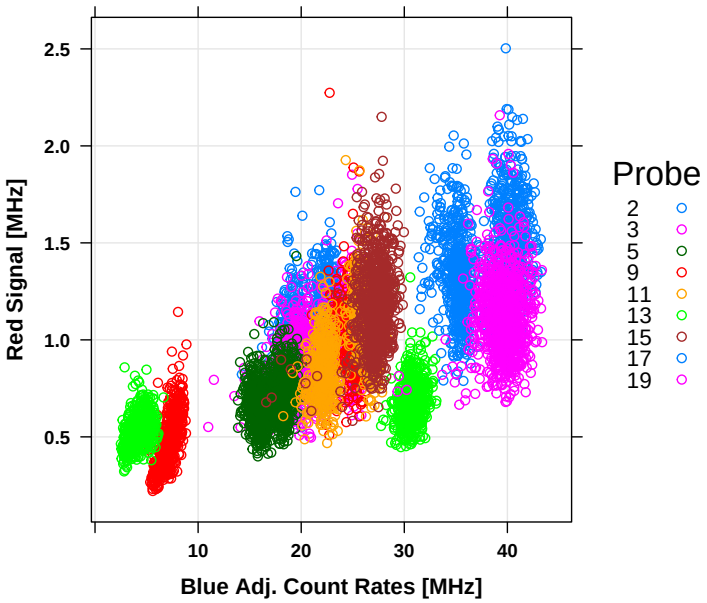

Figure 5.21.: Trackwise plot of blue adjusted count rates and red signal for both readout areas together after irradiation with C12.

5.3.6. Red background vs blue signal

The background signal correlated to the blue signal can be seen in Fig. 5.22. The graph yields a linear correlation in both areas for the most detectors. Therefore it seems possible to estimate the red background from the blue signal. The correlation for ions is depicted in Fig 5.23.

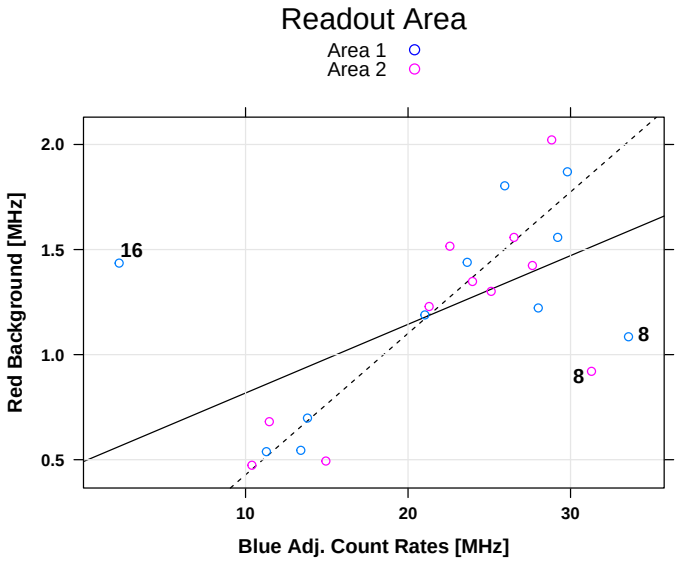

Figure 5.22.: Red adj. count rates before irradiation (background) plotted against blue adj. count rates after irradiation with photons. Dashed line: linear fit excluding the numbered detectors 8 and 16.

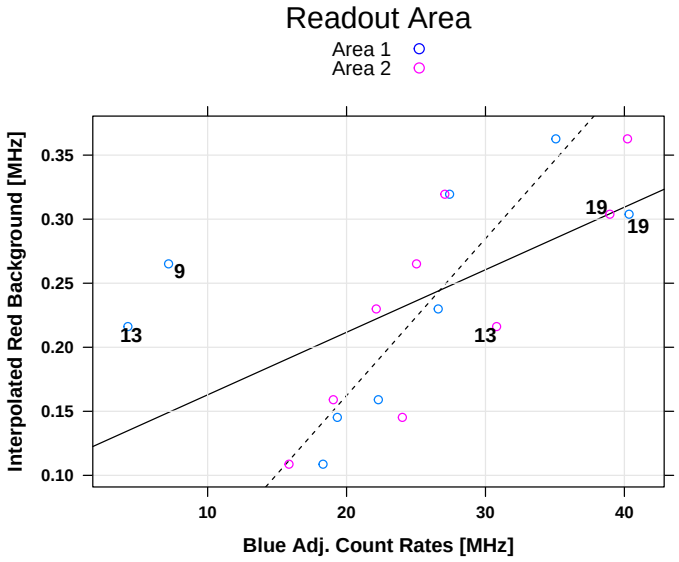

Figure 5.23.: Interpolated mean red track background per image plotted against the blue adj. count rate after irradiation with C12.

6. Discussion

6.1. Basic Characteristics of Emission

6.1.1. Laser power and stability

The laser can be regarded as stable. Its low variations of about 3%, *i.e.* approx. 2 μW, are visible only on a time scale of an hour. Therefore they are neglectable for single images which take maximum a few minutes for acquisition. However, for longer image series it might be possible to see an effect of the changing laser power.

6.1.2. Linearity with laser power and dwell time

In Fig. 6.1 is depicted the relation of adj. count rates, dwell time and laser power [S. Greilich, pers. comm] for the red channel. The signal deviates from the black curve which represents a linear behavior. Instead, it decreases linearly between 1-100% and depends on dwell time. In comparison to this, measurements for the blue channel show that non-linearities in the relation between laser power, dwell time and adjusted count rate can be neglected. This confirms the applicability of the concept of adjusted count rates for the blue channel.

6.2. Photochromatic transformation by blue laser

6.2.1. Depletion of blue Signal

The effect was for both laser powers below 1%. However, in Fig.5.3 the signal decrease for 10% laser power is so small, that a readout is possible essentially without inducing a significant change in blue signal. Regarding the 3% laser power, higher count rates are likely to be produced by the laser instabilities. For this laser power the 2PA is not significant so that the a possible signal decrease over time is smaller than other factors, *e.g.* mechanical stability, laser etc.
As the number of measurements corresponds to a number of rescans R, it can be introduced the product $R \cdot p$, which is to some extend a dimensionless measure of total energy deposited in the detector [15]. Hence, the results can be directly compared to Fig. 3.6. For the in this experiment delivered "energy" of 800 a.u. Hoofs results agree nicely with the 1% decrease observed for the blue signal in this experiment.

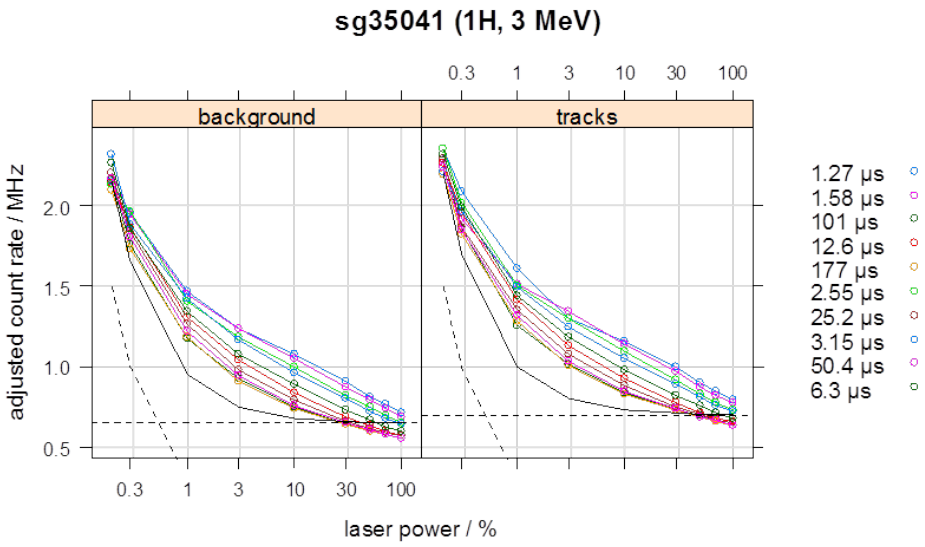

Figure 6.1.: Non-linearity of adj. count rate with dwell time and laser power in the red channel. The black curve is the sum of the dashed lines, which are the expected backgrounds (room light/FNTD). If there was a linear correlation the expected result would match with the black curve. [S. Greilich, pers. comm]

6.2.2. Red Time Series

For a better comparison the graphs in Fig. 5.4 were matched (Fig. 6.2). It becomes clearly visible that the signal of 100% laser power decreases faster than the 30% signal and that there is no simple correction factor between both curves. This is already a first hint towards a laser induced effect. However, the curves non-exponential behavior indicates that there is more than one component present in the signal decrease.

6.2.3. Interrupted Read-Out

We saw that during laser shut-off the res signal remains stable and only changes during readout. This supports the idea of a laser induced effect. However, other effects have to be considered such as the laser caused temperature-rise.
The effect give rise to the conclusion that the signal background relation, measured by Hoof and mentioned before (see Fig. 3.6), can be regarded as maximal estimation of the 2PA induced red signal.

6.2.4. Readout after photon irradiation

The signal increase exceeds by far the laser induced signal reduction, if there is any. Although, the effect seems still significant (2% decrease from signal maximum) it is much smaller for irradiation induced than for 2PA induced signals. The wiggles in

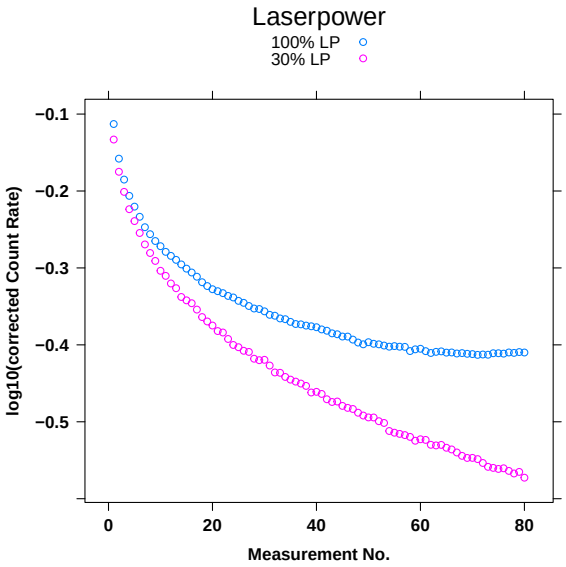

Figure 6.2.: Corrected time curves of 30% and 100% red time series.

the environment of the maximum are likely to reflect microscope variations mentioned before (Sec. 5.1.1). It seems plausible that the irradiation effects extend until several minutes after actual irradiation and that laser induced retransformations appears just after irradiation induced processes finish. Nonetheless the reason of this effect is yet unclear and so are its implications for dosimetry. A modification of the assumed band model (Fig 3.3) might be necessary. The model could also be corrected in a way that the color center concentration stays constant but the factors α and β are functions of energy, which could also be related to the non-linearity of adj. count rates and laser power in the red channel. Another interesting question would be if this effect is also seen when reading out a irradiated sample from longer term storage with a time series.

6.2.5. Signal Ranges and dose response

Photon response curves

The resulting blue curve exhibits some features similar to the red response curve. Both show saturation effects. For low doses the blue curve seems to have a constant maximum value. In the red channel this effect is exactly inverse. As expected the blue curve has a negative slope in between the plateaus, where the red signal increases. Fig. 6.3 shows the red response as published previously by group [3]. It confirms the behavior seen in the measured red curve. These observations support a two compartment model. But a closer look at the adj. count rates of the blue channel (Tab. 5.1) reveals that for high doses the rates are still around 10 MHz and they seem to keep decreasing. However, the red adj. count rates are saturated. This is a contradiction to the two compartments model as their seems to be at least one more compartment to where the blue color centers are

transformed when the red color centers are saturated.
The plot of the ratio of the a priori concentrations of color centers converged towards 0.3%. This states that the blue color center concentration in an unirradiated FNTD can be regarded as total color center concentration. This estimation is possible until approx. 10 Gy, when the conversion ratio starts to increase. The Γ-value is only for high doses significant since here $\Delta\Gamma$ becomes an order of magnitude smaller than Γ. This is because the simple approach to regard the 0 Gy sample as background, is only valid for high conversion rations. Furthermore the real background can be very different and therefore this calculation allows only a estimation of Γ.
The span of observed adj. count rates in the red channel exceeds the blue channel range by far, meaning that even after irradiation with 10 kGy there is still a significant amount of untransformed color centers present in the crystal. This is represented by conversion ratios for high doses of about 76% in the blue and max. 260% in the red channel and it states that transformation of blue color centers continues. This yields the question whether high dose measurements are feasible in the blue channel.

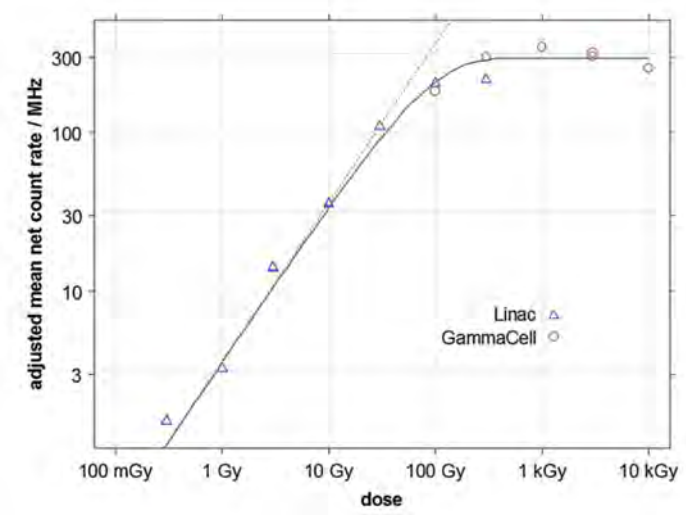

Figure 6.3.: Red photon response curve (from [3]).

Convertion Ratio for Ions

On the blue channel Xe-tracks image in Chapter 3 (Fig. 3.5 a)the tracks appear as dark spots. In spite of rescanning 8 times this already shows, that an important amount of blue color centers must have been transformed. The conversion ratio turned out to be around 40%. Signals of ion tracks can be estimated to around 5.5 MHz. The adj. count rate for the foreground is around 14 MHz and hereby below the range seen for the unirradiated 20 detectors in Tab.5.7. However, it is in the range of blue signals of irradiated detectors. This could mean, on the one hand that this low value cannot be explained by intersample color center concentration variation and on the other hand,

that maybe it is not possible to invert the results of the "background subtractor" to interpolate an unirradiated blue signal.

6.3. Correlation experiments

6.3.1. Coloration and blue signal

As seen in all correlation plots in chapter 5 the detectors 8 and 19 exhibit extremely high signals in the blue channel. As mentioned before there is a small correlation between absorption and blue signal which even becomes significant (p-value = 0.00022) when excluding samples 8 and 19 from the linear model (dashed line). However, this correlation is not practically useful, since blue signal varies a lot. Therefore absorption, as determined in this work, is not a good measure for the blue color center concentration. A problem was the absorption measurement itself. The wellplate reader is built to measure liquids. By inserting a solid absorber in the machine and selecting a well plate model, the effective absorption path does not correspond to the path used by the machine. Though, this systematic error should affect all measurements equally so that at least a relative statement can be obtained. Nevertheless because of lack of knowledge about the apparatus, we must assume a great uncertainty for the measured absorption.

6.3.2. Intrasample Variation of blue signal

We have seen that the variation of blue color center concentration within the same detector is smaller than between different detectors. The linear fit is significant (p-value of $6.85 \cdot 10^{-11}$) and has a slope of 0.916. Especially the values with adj. count rated between 40 MHz and 50 MHz in Area 1 cause a deviation from the angle bisector.

6.3.3. Blue signal before and after irradiation

Blue signals before and after irradiation are significantly correlated for both, photon and carbon irradiated detectors. The correlation becomes even better, when excluding the numbered detectors. As seen in Fig 5.13 and 5.14 detectors 8 and 19 already yielded a outstanding high blue signal before irradiation. They had to be measured with a lower laser power. Because, according to the results of Sec. 5.1, this should have no influence on the adjusted count rates, the reason for the high adj. count rates is yet unclear. In contrast, the ten times lower value of the area 1 readout of detector 16 can be explained. Here the sample laid in an inclined position and so the blue image was taken not within the detector but on its surface. Hence, this value was also excluded. The same effect could possibly explain the low area 1 values of detectors 9 and 13.
The here for photons calculated red conversion ratio χ_{red} is one order of magnitude smaller than the one estimated for photons in Sec. 5.2.5 for the same dose of 100 Gy (see Tab. 5.2). However, χ_{blue} is in the same range as in Tab. 5.1. As a consequence also the ratio of a priori color center concentrations Γ is an order of magnitude higher in this

measurement than in the previous one. A possible explanation could be the non-linear relation of laser power, dwell time and adj. count rate in the red channel. Detectors in Sec. 5.2.5 were readout with 1% relative laser power, whereas here 10% were used. Nevertheless this discrepancy could also indicate a dose dependency of Γ, which would mean that the two components model has to be revised.

6.3.4. Intrasample red and blue signal correlation

In a track by track comparison the Poisson noise and/or microscope sensitivity change over the image are too strong to see any features. After sufficient averaging a significant correlation between red and blue signal becomes evident (p-value = 2.56e-08 for Fig. 5.18). This implies for the application of the blue signal that it can be used as sensitivity correction.

6.3.5. Sensitivity vs. blue signal

The experiments showed that after irradiation of the FNTD the red signal of both kinds of radiation is correlated to the blue channel signal. The correlation is significant (p-value (photons) = 0.00686, p-value(ions) = $1.65 \cdot 10^{-5}$). The dashed lines in Fig. 5.19 and 5.20 represent linear fits, excluding the problematic FNTDs mentioned above. This increases the significance level.
Although the trackwise plot could affirm the linear correlation of the mean values per area, it also depicted, that due to a strong spread of data points, this correlation is no longer feasible on a local scale.

6.3.6. Red background vs. blue signal

We saw that the red background and blue signal of both radiations correlate significantly. Again this could be improved by excluding the numbered detectors (dashed lines, p-value (photons) =$4.15 \cdot 10^{-8}$, p-value(ions) =$7.71 \cdot 10^{-5}$. This means that it is possible to deduce the red background by a extra blue channel readout. Correlation for photons is better than for ions. This might be due to the fact that the ion background was calculated by the background subtractor whereas for photons it was measured.
The fact that the blue signal is correlated as well to the red sensitivity as to the red background claims, that also red signal and background are correlated. This could not be recognized by Hoof, as he considered only local scales (*i.e.* single images). But because of the noise seen in the sections above, the correlation only becomes visible in intersample (or intrasample but interimage) considerations. Hence, a normalization of the red signal using the background is possible only when comparing different images/samples.

7. Conclusion and Outlook

In this work the feasibility of employing the hitherto unused blue-greenish fluorescence (blue channel) for quantification and normalization was investigated. Also, the correlation of transformed and untransformed color center concentration to detector sensitivity was assessed. The objects of investigation were mainly 20 hand-selected FNTDs which represented the range of coloration found during the crystal growth process.
It was found that with a sufficient low laser power (below 10% relative laser power of 458 nm Ar-laser) it is feasible to read out the blue channel consistently and apply the adj. count rate concept. The blue signal in an unirradiated crystal was found to be a good measure for the total color center concentration. Further it was seen, that the response to photon radiation of the blue channel is widely inverse to the red channel, what supports the assumed two compartment model, consisting of only transformed (red) and untransformed (blue) color centers. In the blue channel the signal range in terms of adj. count rates is within 40 MHz to approximate 10 MHz and thus smaller than in the red channel (0.5 MHz to $\approx$ 260 MHz). Together with the range of ratios of a priori color center concentrations Γ ($0.3 > \Gamma > 0.03$) this indicates that the concentration of blue color centers exceeds the red color center concentration by far. However, the blue response to photon radiation seems to have not reached saturation yet, whereas the red signal (sensitivity to dose) is saturated. This indicates a least a partial failure of the model. The comparison between Γ for the photon response and the 11 photon irradiated detectors of Sec. 4.3.3 yielded a possible dose dependency of Γ supporting the failure of the model.
Another important observation was that the red signal and the red background are both correlated to the blue signal and hereby correlated to each other. This means that not only the blue signal, but also the red background is a good measure for signal normalization. The correlation is though limited by intrasample noise to an intersample comparison and was therefore not seen clearly in previous studies [15]. In contrast, the optical absorption of the FNTDs as determined in this study yielded not to be suitable as replacement for blue channel measurements.
A new laser dependent instability of red signal after 2PA was discovered with yet unclear implications for dosimetry. Together with the partial failure of the two compartment model this implies a modification of the current band model (Fig. 3.3) considering more complex transformation routes, which could maybe also explain the observed irregularities for a small subset of the FNTDs used here.

A continuation of this project could imply a better quantification of the observed effects by improving the experiments statistics (*e.g.* by more samples). Also, the unsaturated blue signal response gives rise to the idea of higher dose measurements using the

blue channel. It terms of signal correlations it should be assessed whether a measurement of the blue/green emission is necessary or whether the correlation of red background and red signal is sufficient for signal normalization. Regarding the possibility of local red signal normalization, the high noise is probably partly caused by microscope parameters. The correlation measurements could be repeated, once a flat-field correction for the microscope is available.

Appendices

A. Results of correlation measurements with 20 FNTDs

FNTD Nr.	Radiation	Normalized Absorption	Adj. Count Rates Blue Channel [MHz]				Adj. Count Rates Red Channel [MHz]			
			Unirradiated		Irradiated		Unirradiated		Irradiated	
			Area 1	Area 2	Area 1	Area 2	Area 1	Area 2	Area 1	Area 2
1	gamma	6,120	26,238	24,509	11,282	10,392	0,538	0,474	10,481	10,195
2	12C	5,846	33,035	33,021	22,288	19,046	0,159	0,159	1,093	0,983
3	12C	5,714	27,577	28,111	19,335	24,018	0,145	0,145	0,861	0,991
4	gamma	5,170	23,224	21,449	13,400	14,943	0,545	0,494	13,004	14,614
5	12C	5,808	26,089	25,854	18,306	15,856	0,109	0,109	0,732	0,650
6	gamma	7,491	48,384	50,855	28,014	27,654	1,222	1,424	21,701	21,862
7	gamma	7,319	43,375	44,055	25,951	26,520	1,803	1,558	18,676	21,018
8	gamma	6,402	69,289	62,276	33,568	31,290	1,085	0,920	15,321	15,892
9	12C	6,102	44,767	39,164	7,186	25,036	0,265	0,265	0,485	1,023
10	gamma	7,476	40,020	43,431	23,642	22,575	1,439	1,516	16,337	16,058
11	12C	7,078	48,617	39,227	26,598	22,137	0,230	0,230	1,061	0,844
12	gamma	5,907	34,655	37,397	21,035	23,967	1,189	1,348	16,406	18,329
13	12C	6,478	45,847	40,849	4,258	30,801	0,216	0,216	0,534	0,681
14	gamma	6,081	30,123	28,214	13,811	11,463	0,698	0,681	13,584	11,680
15	12C	5,315	41,609	38,831	27,417	27,074	0,319	0,319	1,160	1,175
16	gamma	7,689	49,332	42,486	2,221	21,298	1,436	1,229	1,638	14,724
17	12C	8,126	47,315	47,553	35,064	40,225	0,363	0,363	1,346	1,496
18	gamma	6,832	45,098	39,469	29,807	28,840	1,870	2,022	21,445	21,038
19	12C	5,612	73,167	74,486	40,338	38,955	0,304	0,304	1,125	1,124
20	gamma	6,388	46,701	37,905	29,209	25,116	1,558	1,301	20,794	18,675

Figure A.1.: Results of the measurements with 20 FNTDs

List of Figures

List of Tables

Bibliography

[1] Dieter Schardt, Thilo Elsässer, and Daniela Schulz-Ertner. Heavy-ion tumor therapy: Physical and radiobiological benefits. *Rev. Mod. Phys.*, 82:383–425, Feb 2010.

[2] Mark S. Akselrod and Garrett J. Sykora. Fluorescent nuclear track detector technology - A new way to do passive solid state dosimetry. *Radiation Measurements*, 46(12):1671–1679, December 2011.

[3] Steffen Greilich, Julia.-M. Osinga, Martin Niklas, Florian M. Lauer, Grischa Klimpki, Felix Bestvater, James A Bartz, Mark S Akselrod, and Oliver Jäkel. Fluorescent Nuclear Track Detectors as a Tool for Ion-Beam Therapy Research. *Radiation Measurements*, in press, 2013.

[4] Report 85. *Journal of the ICRU*, 11(1):NP, 2011.

[5] J. M. Osinga. *Fluorescent Nuclear Track Detectors: High-Accuracy Fluence Determination in Ion Beams.* Master's thesis, Martin Luther University of Halle-Wittenberg, Germany, 2012.

[6] G. Blasse and B.C. Grabmaier. *Luminescent Materials.* Springer-Verlag, Berlin, Heidelberg, 1994.

[7] J. B. Pawley, editor. *Handbook of biological confocal microscopy.* Springer Science Business Media, Berlin, Heidelberg, 3rd edition, 2006.

[8] Mark S. Akselrod, Anna E. Akselrod, Sergei S. Orlov, Subrata Sanyal, and Thomas H. Underwood. New aluminum oxide single crystals for volumetric optical data storage. *Optical Data Storage*, 5069:244–250, 2003.

[9] Mark S. Akselrod and Anna E. Akselrod. New Al2O3:C,Mg crystals for radiophotoluminescent dosimetry and optical imaging. *Radiation Protection Dosimetry*, 119(1-4):218–221, January 2006.

[10] Mark S. Akselrod, Anna E. Akselrod, Sergei S. Orlov, Subrata Sanyal, and Thomas H. Underwood. Fluorescent Aluminum Oxide Crystals for Volumetric Optical Data Storage and Imaging Applications. *Journal of Fluorescence*, 13(6):503–511, November 2003.

[11] Mark S. Akselrod, Sergei S. Orlov, and Gleb M. Akselrod. Bit-Wise Volumetric Optical Memory Utilizing Two-Photon Absorption in Aluminum Oxide Medium. *Japanese Journal of Applied Physics Physics*, 43(7B):4908–4911, 2004.

[12] Carl Zeiss MicroImaging GmBH. *ZEN 2009 LSM 710 and ConfoCor 3: Operating Manual*, 2009.

[13] W. S. Rasband. *ImageJ.* U.S. National Insitutes of Health, Bethesda, Maryland, USA, URL: http://rsb.info.nih.gov/ij/ (2013) .

[14] R Development Core Team. *R: A language and environment for statistical computing.* R Foundation for Statistical Computing, Vienna, Austria, 2013.

[15] S. Hoof. *Correlation of Particle and Background Signal in Al_2O_3:C,Mg Fluorescent Nuclear Track Detectors.* Bachelor's thesis, Ruprecht-Karls-University Heidelberg, Germany, 2013.

[16] R. Martel. *Werkzeuge zur Untersuchung des Hintergrundes von fluoreszierenden Kernspurdetektoren.* Bachelor's thesis, Ruprecht-Karls-University Heidelberg, Germany, 2012.

[17] Julia-M. Osinga, Mark S. Akselrod, Rochus Herrmann, Volker Hable, Günter Dollinger, Oliver Jäkel, and Steffen Greilich. High-Accuracy Fluence Determination in Ion Beams using Fluorescent Nuclear Track Detectors. *Radiation Measurements*, in press, 2013.

Acknowledgements

My profound gratitude goes to all the people at the German Cancer Research Center (DKFZ) that helped and supported me and without whom this bachelor project would not have been possible.

First, I would like to express my gratitude to Prof. Dr. Wolfgang Schlegel, head of the Department of Medical Physics in Radiation Oncology at DKFZ, for giving me the opportunity to work in his research division. I would like to thank Prof. Dr. Oliver Jäkel for accepting me in his research group, where I gained insight in the fascinating field of medical physics in general and in special heavy ion therapy. Furthermore, I want to thank Prof. Dr. Peter Bachert for accepting to be my first referee and the representative of the Department of Physics and Astronomy of the University of Heidelberg.

My special thanks go to the Heavy Ion Therapy Research Group, before all to Dr. Steffen Greilich for being an excellent supervisor and guide during the last months. I deeply appreciate all his advices and encouragements and thank him for his tremendous dedication. I would also like to thank the whole group for a nice working atmosphere and entertaining lunch and coffee brakes. The FNTD people, namely Julia-Maria Osinga, Martin Niklas and Nicolas Schudell, I thank for all their useful advices and their help with measurements. Without this a realization of this work in the given time would not have been possible. I am also thankful to them and Nora Hühnemohr for proofreading this thesis. Other special thanks goes to Sonja Schellhammer who accompanied my way through the DKFZ and who shared with me many moments of desperation and joy during this whole time, but especially during the writing process. Laughing together was a welcome change in desperate moments.

Furthermore I thank the DKFZ light microscopy facility for readout times and Dr. Mark S. Akselrod and Dr. James Bartz from Laundauer Inc. for supplying us with FNTDs, especially with the set of 20 hand-selected FNTDs. Another person I would like to mention is Ivana Dokic form the Department of Tumorvirology at DKFZ. Only thanks to her uncomplicated help I was able to perform the absorption measurements. Also thanks to Andrea Schwahofer from DKFZ and Dr. Stephan Brons from HIT for enabling the irradiations.

Last but not least, I want to thank my family and my friends. My family, for being patient, having consideration and clearing by back in the last weeks. Without their tremendous support I would not have been able to finish this work in given time. My friends, for being comprehensive and for cheering me up and encouraging me whenever it was necessary.

Declaration

Ich versichere, dass ich diese Arbeit selbstständig verfasst und keine anderen als die angegebenen Quellen und Hilfsmittel benutzt habe.

Heidelberg, den 08. August 2013